

1 **Modelling the firn thickness evolution during the last deglaciation:** 2 **constraints on sensitivity to temperature and impurities**

3
4 Camille Bréant ^{1,2}, Patricia Martinerie ², Anaïs Orsi ¹, Laurent Arnaud ² and Amaëlle Landais ¹

5
6 ¹Laboratoire des Sciences du Climat et de l'Environnement, UMR8212, CEA-CNRS-UPS/IPSL, Gif-sur-Yvette,
7 France

8 ²Univ. Grenoble Alpes, CNRS, IRD, IGE, UMR5001, Grenoble, F-38000, France

9
10 The transformation of snow into ice is a complex phenomenon which is difficult to model.
11 Depending on surface temperature and accumulation rate, it may take several decades to millennia
12 for air to be entrapped in ice. The air is thus always younger than the surrounding ice. The resulting
13 gas-ice age difference is essential to document the phasing between CO₂ and temperature changes
14 especially during deglaciations. The air trapping depth can be inferred in the past using a firn
15 densification model, or using $\delta^{15}\text{N}$ of air measured in ice cores.

16 All firn densification models applied to deglaciations show a large disagreement with $\delta^{15}\text{N}$
17 measurements in several sites of East Antarctica, predicting larger firn thickness during the Last
18 Glacial Maximum, whereas $\delta^{15}\text{N}$ suggests a reduced firn thickness compared to the Holocene. Here
19 we present modifications of the LGGE firn densification model, which significantly reduce the
20 model-data mismatch for the gas trapping depth evolution over the last deglaciation at coldest sites
21 of East Antarctica (Vostok, Dome C), while preserving the good agreement between measured and
22 modelled modern firn density profiles. In particular, we introduce a dependency of the creep factor
23 on temperature and impurities in the firn densification rate calculation. The temperature influence
24 intends to reflect the dominance of different mechanisms for firn compaction at different
25 temperatures. We show that both the new temperature parameterization and the influence of
26 impurities contribute to the increased agreement between modelled and measured $\delta^{15}\text{N}$ evolution
27 during the last deglaciation at sites with low temperature and low accumulation rate, such as Dome
28 C or Vostok. We find that a very low sensitivity of the densification rate to temperature has to be
29 used in coldest conditions. The inclusion of impurities effects improves the agreement between
30 modelled and measured $\delta^{15}\text{N}$ at cold East Antarctic sites during the last deglaciation, but
31 deteriorates the agreement between modelled and measured $\delta^{15}\text{N}$ evolution in Greenland and
32 Antarctic sites with high accumulation unless threshold effects are taken into account. We thus do
33 not provide a definite solution to the firnification at very cold Antarctic sites but propose potential
34 pathways for future studies.

35

36 1. Introduction

37

38 Ice cores are important tools to decipher the influence of different forcings on climate evolution.
39 They are particularly useful to reconstruct the past variations of polar temperature and greenhouse
40 gases. The longest record covers 8 last glacial – interglacial cycles (EPICA community members,
41 2004; Jouzel et al., 2007; Loulergue et al., 2008; Lüthi et al., 2008) and very high resolution climate
42 records can be retrieved from ice cores drilled in high accumulation regions (Marcott et al., 2014;
43 Rhodes et al., 2015; WAIS Divide Project Members, 2013, 2015).

44

45 Polar ice is a porous medium, and contains bubbles filled with ancient atmospheric air, allowing the
46 reconstruction of the atmospheric composition in the past. The air is trapped at about 50-120 m
47 under the ice sheet surface. Above that depth, the interstitial air in firn pores remains in contact
48 with the atmosphere. Consequently, the air is always younger than the surrounding ice and this age
49 difference, Δ_{age} , can reach several millennia at the low temperature and accumulation rate sites of
50 East Antarctica.

51

52 A precise determination of Δ_{age} is essential to quantify the link between temperature changes
53 recorded in the water isotopic measurements on the ice phase and greenhouse gas concentrations
54 recorded in the gas phase. Still, quantifying the temporal relationship between changes in
55 greenhouse gas concentrations in air bubbles and changes in polar temperature recorded in the
56 isotopic composition of the ice is not straightforward. One way to address this question goes
57 through the development of firn densification models that depict the progressive densification of
58 snow to ice, and the associated decrease of porosity. Below a certain threshold density, the pores
59 seal off and the air is trapped. The firn densification models thus calculate the Lock-in Depth
60 (hereafter LID) according to surface climatic conditions. A higher temperature accelerates the firn
61 metamorphism and leads to a shallower LID. On the other hand, a higher snow accumulation at the
62 surface will have the effect of increasing the firn sinking speed and hence deepening the LID.

63 On glacial – interglacial timescales, increasing temperature is associated with increasing snow
64 accumulation. Indeed, the thermodynamic effect dominates when dealing with long term averages
65 (several thousands of years), even if accumulation and temperature are not always correlated on
66 millennial and centennial timescale in polar regions, especially in coastal areas (e.g. Fudge et al.,
67 2016; Altnau et al., 2014). As a consequence, we observe for all available ice cores covering the last

68 deglaciation joint increases in both accumulation and temperature. In the firn densification model,
69 both effects partially compensate each other, with the temperature effect being dominant in the
70 current densification models for the LID simulation over glacial – interglacial transitions in deep
71 drilling sites of the East Antarctic plateau, hence leading to the modelled LID decrease.

72 A first class of densification models is based on an empirical approach to link accumulation rate and
73 temperature at different polar sites to densification rates (allowing the match between the
74 modelled and the measured density profiles) (e.g. Herron and Langway, 1980). The Herron and
75 Langway (1980) model assumes that the porosity (air space in the firn) variations directly relate to
76 the weight of the overlying snow, hence the accumulation rate. A temperature dependence
77 following an Arrhenius law is also implemented to account for a more rapid compaction at higher
78 temperature. Finally, the exact model sensitivity to temperature and accumulation rate is adjusted
79 empirically in order to simulate observed density profiles. Measured density profiles exhibit
80 different densification rates above and below 550 kg/m^3 so that different empirical laws are used
81 for densities above and below this threshold. Indeed, 550 kg/m^3 corresponds to the observed
82 maximum packing density of snow (e. g. Anderson and Benson, 1963), hence to a change in the
83 driving mechanism of firnification.

84
85 Despite its simple empirical description, and although more sophisticated empirical models have
86 been developed (Arthern et al., 2010; Helsen et al., 2008; e.g. Li and Zwally, 2004; Ligtenberg et al.,
87 2015), the Herron and Langway (1980) firn model often provides good quality results and is still used
88 in a number of ice core studies (e.g. Buizert et al., 2015; Overly et al., 2015, Lundin et al., 2017).
89 However, its validity is questionable when used outside of its range of calibration, such as glacial
90 periods at cold sites of the East Antarctic plateau for which no present-day analogue exists. As a
91 consequence firn models including a more physical description of densification have been
92 developed (e.g. Arnaud et al., 2000; Salamatin et al., 2009). The model developed over the past 30
93 years at LGGE (Arnaud et al., 2000; Barnola et al., 1991; Goujon et al., 2003; Pimienta, 1987) aims
94 at using a physical approach which remains sufficiently simple to be used on very long time scales
95 (covering the ice core record length). More complex models, explicitly representing the material
96 micro-structure have been developed but require a lot more computing time (Hagenmuller et al.,
97 2015; Miller et al., 2003). Still, the simplified physical mechanisms in our model include parameters
98 adjusted through comparison of modelled and measured present-day firn density profiles which
99 may induce biased results outside the range of calibration.

100

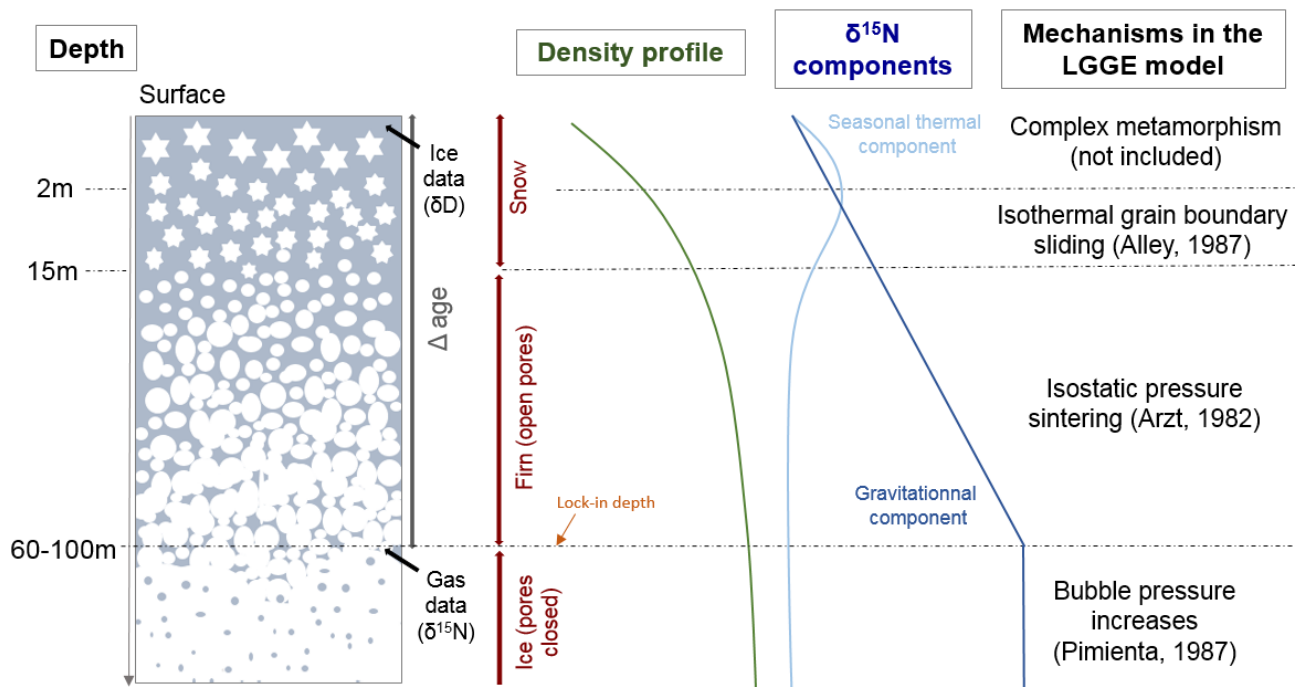
101 In parallel to firn densification modelling, past firn LID can also be determined using the $\delta^{15}\text{N}$
102 measurements in the air trapped in ice cores. Indeed, in the absence of transient thermal gradients,
103 the $\delta^{15}\text{N}$ trapped at the bottom of the firn is mainly related to the diffusive column height (DCH).
104 This is due to gravitational settling in the firn following the steady state barometric equation (Craig
105 et al., 1988; Schwander, 1989; Sowers et al., 1989):

$$107 \quad \delta^{15}N_{grav} = \left[\exp\left(\frac{\Delta mgz}{RT_{mean}}\right) - 1 \right] 1000 \approx \frac{gz}{RT_{mean}} \Delta m \times 1000 \text{ (‰)} \quad (1)$$

108
109 Where Δm is the mass difference (kg/mol) between ^{15}N and ^{14}N , g is the gravitational acceleration
110 (9.8 m/s^2), R is the gas constant (8.314 J/mol/K), T_{mean} is the mean firn temperature (K), and z is the
111 diffusive column height noted (DCH). In the absence of convection at the top of the firn, the firn LID
112 is equal to the DCH.

113
114 In Greenland ice cores, where strong and abrupt surface temperature changes occurred during the
115 last glacial period and deglaciation, $\delta^{15}\text{N}$ is also affected by strong thermal fractionation. An abrupt
116 warming (on the order of 10°C in less than 50 years) indeed induces a transient temperature
117 gradient in the firn of a few degrees (Severinghaus et al., 1998; Guillevic et al., 2013; Kindler et al.,
118 2014). $\delta^{15}\text{N}$ is thus modified as $\delta^{15}\text{N}_{therm} = \Omega \cdot \Delta T$, where Ω is the thermal fractionation coefficient
119 (Grachev and Severinghaus, 2003) and this thermal signal is superimposed on the gravitational one
120 (the $\delta^{15}\text{N}_{therm}$ observed is in most cases lower than 0.15‰).

121



122

123

124 *Figure 1: Overview of snow densification and influence on the $\delta^{15}\text{N}$ profile in the absence of any significant convective*
 125 *zone as observed in most present-day $\delta^{15}\text{N}$ profiles (Landais et al., 2006; Witrant et al., 2012).*

126

127 While models can reproduce the observed $\delta^{15}\text{N}$ at Greenland sites over the last climatic cycle, a
 128 strong mismatch is observed for cold Antarctic sites, especially on the East-Antarctic plateau
 129 (Dreyfus et al., 2010). In particular, both the empirical and physical models predict a decrease of the
 130 LID during glacial to interglacial transitions (Goujon et al., 2003; Sowers et al., 1992) while the $\delta^{15}\text{N}$
 131 evolution indicates an increase of the LID (Capron et al., 2013; Sowers et al., 1992). The decrease in
 132 the LID in the models is caused by the increase in temperature during the deglaciation, which has a
 133 stronger impact than the increase in the accumulation rate. The differences in modelled and
 134 measured $\delta^{15}\text{N}$ for glacial periods in cold sites of the East-Antarctic plateau have important
 135 consequences for the Δage estimate and hence the ice core chronology: using the firn densification
 136 models, the modelled Δage for glacial period at Vostok and Dome C is too large by several centuries
 137 (Loulergue et al., 2007; Parrenin et al., 2012).

138 Several hypotheses have already been invoked to explain the $\delta^{15}\text{N}$ model-data mismatch in
 139 Antarctica as detailed in Landais et al. (2006), Dreyfus et al. (2010) and Capron et al. (2013). First,
 140 the firnification models have been developed and tuned for reproducing present-day density
 141 profiles and it is questionable to apply them to glacial climate conditions in Antarctica for which no
 142 present-day analogues are available. Second, increasing impurity concentration has been suggested
 143 to fasten firn densification during glacial period (Freitag et al., 2013; Hörhold et al., 2012). Third, a

144 ~20 m deep convective zone has been evidenced in the megadunes region in Antarctica
145 (Severinghaus et al., 2006) hence suggesting that deep convective zones can develop in glacial
146 periods in Antarctica and explain the mismatch between firn densification model and $\delta^{15}\text{N}$ data
147 (Caillon et al., 2003). This hypothesis can explain the mismatch between modelled and measured
148 $\delta^{15}\text{N}$ at EDML during glacial period by invoking a 10 m convective zone (Landais et al., 2006).
149 However, it has been ruled out for explaining the strong mismatch between model and $\delta^{15}\text{N}$ data at
150 EDC for the last glacial period (Parrenin et al., 2012). Fourth, firn densification is very sensitive to
151 changes in temperature and accumulation rate so that uncertainties in the surface climate
152 parameters can lead to biased value of the modelled LID and hence $\delta^{15}\text{N}$. Fifth, a significant thermal
153 fractionation signal can affect the total $\delta^{15}\text{N}$ signal. However, this hypothesis has been ruled out by
154 Dreyfus et al. (2010) based on $\delta^{15}\text{N}$ and $\delta^{40}\text{Ar}$ data on the last deglaciation at EDC.

155

156 In this study, we test whether simple modifications of the LGGE model can reduce the model-data
157 mismatch for the LID evolution over the last deglaciation in sites on the East Antarctic plateau. In
158 particular, it has been suggested by Capron et al. (2013) that the firn densification rate is
159 underestimated at very low temperature. We also examine the possible influence of impurity
160 concentration in the LGGE model following the approach by (Freitag et al., 2013; Hörhold et al.,
161 2012). The manuscript is organized as follows. In the next (second) section we present the physical
162 model with a focus on recent modifications. In a third section, we confront the model output to
163 present-day observed firn density profiles and $\delta^{15}\text{N}$ data over the last deglaciation at different polar
164 sites from Greenland and Antarctica. Section 4 summarizes our conclusions.

165

166 2. Densification model description and improvements

167

168 An in-depth description of the LGGE firn densification model is provided in Goujon et al. (2003).
169 Here we first briefly summarize its content, and then detail the modifications introduced in this
170 study. The main inputs to the model are temperature and snow accumulation rate (Supplementary
171 Text S1). During climatic transitions occurring at similar or shorter time scales than firnification, the
172 propagation of the atmospheric temperature signal into the firn has to be taken into account
173 (Schwander et al., 1997). The thermo-mechanical model comprises four modules. A simple ice sheet
174 flow module calculates the vertical speed in a 1D firn and ice column. This vertical speed is used in
175 the thermal module to calculate heat advection. The thermal module solves the heat transfer
176 equation, which combines heat advection and heat diffusion across the whole ice-sheet thickness.

177 Using the resulting temperature profile in the firn, the mechanical module evaluates the
178 densification rates resulting from three successive mechanisms detailed below. Finally, a gas-age
179 module keeps track of snow layers sinking in a Lagrangian mode and uses a gas trapping criterion in
180 order to evaluate the gas trapping depth and the ice age – gas age difference (Δ age).

181 The model does not take into account the complex mechanisms associated with snow
182 metamorphisms under the influence of strong temperature gradients, wind and sublimation/re-
183 condensation (Colbeck, 1983; Kojima, 1967; Mellor, 1964). This kind of metamorphism affects the
184 1-3 meters at the top of the firn and has a minor role on the modelled LID.

185 Below this depth, the densification of snow into ice has been divided into three stages (e.g. Maeno
186 and Ebinuma, 1983 and references therein; Figure 1). The first stage, named “snow densification”
187 as in Goujon et al. (2003), corresponds to a rearrangement and packing of snow grains until
188 approaching the maximum compaction at a density of about 550 kg/m^3 (or 0.6 on a unitless scale
189 relative to the density of pure ice) defined as the critical density. The second stage represents the
190 “firn densification” by sintering associated with visco-plastic deformation. Finally, when the bubbles
191 are closed (at a relative density of about 0.9), the ice densification is driven by the difference in
192 pressure between air trapped in bubbles and the solid ice matrix subject to the weight of the
193 overlying firn structure. In reality, the adjacent densification mechanisms likely coexist at
194 intermediate densities. Below we further describe the mechanical structure of the model with a
195 focus on recent modifications and proposed parameterizations. We refer to Arnaud et al. (2000)
196 and Goujon et al. (2003) for more details.

197
198 The model uses macroscopic (simplified) mechanical laws, which link the densification speed
199 (dD_{rel}/dt , in terms of relative density ($D_{rel} = \frac{\rho}{\rho_{ice}}$)) to its main driving force: the overburden
200 pressure of overlying snow. It is important to note that in our model, the accumulation rate
201 influences firn densification only through the overburden pressure:

202

$$203 \quad P(h) = g \int_0^h \rho dz \quad (2)$$

204

205 where g is the gravity constant and ρ is the density in kg/m^3 . This differs from the Herron and
206 Langway (1980) model where the effect of accumulation rate is adjusted and expressed with a
207 different power law for snow and firn densification rates. In porous materials, the overburden
208 pressure P is transmitted through contact areas between grains rather than the entire surface of
209 the material. This is expressed by replacing P with an effective pressure P_{eff} in mechanical stress-

210 strain laws. The relationship between P and P_{eff} depends on the material geometry (e.g. Equation
 211 A4 in Goujon et al., 2003). A higher temperature (T) facilitates the deformation of materials, and
 212 this effect is commonly represented by an Arrhenius law: $e^{\left(\frac{-Q}{RT}\right)}$ where R is the gas constant and Q
 213 an activation energy. The value of the activation energy depends on the underlying physical
 214 mechanism of ice and snow deformation but Arrhenius expressions cannot represent deformation
 215 effects linked to ice melting. The relationships between densification speed and overburden
 216 pressure take the following general form:

217

$$218 \quad \frac{dD_{rel}}{dt} = A_0 \times e^{\left(\frac{-Q}{RT}\right)} \times (P_{eff})^n \quad (3)$$

219

220 where $A_0 = 7.89 \times 10^{-15} \text{ Pa}^{-3} \cdot \text{s}^{-1}$ (Goujon et al., 2003, Eq. A5) and n is the stress exponent. In the rest
 221 of the manuscript, we will refer to $A = A_0 \times e^{\left(\frac{-Q}{RT}\right)}$ as the creep parameter.

222

223 2.1 Densification of snow

224

225 During the first stage, the dominant snow densification mechanism is assumed to be isothermal
 226 boundary sliding and the model of Alley (1987) is used (Figure 1). The geometrical approximation
 227 used to build the model is to represent snow as equal size spheres with a number of contacts
 228 between neighbours increasing with density. In the LGGE model, the Alley mechanism is
 229 implemented as Equation A1 in Goujon et al. (2003):

230

$$231 \quad \frac{dD_{rel}}{dt} = \gamma \left(\frac{P}{D_{rel}^2} \right) \left(1 - \frac{5}{3} \times D_{rel} \right) \quad (4)$$

232

233 It directly relates to Equation (5) in Alley (1987):

234

$$235 \quad \frac{dD_{rel}}{dt} = \frac{2}{15} \times \frac{\lambda}{\nu} \times \frac{R}{r^2} \times \left(1 - \frac{5}{3} * D_{rel} \right) \times \frac{P}{D_{rel}^2} \quad (5)$$

236

237 where λ is the bond thickness, ν the bond viscosity, R the grain radius and r the bond radius. P is
 238 expressed as a function of accumulation and gravity (Equation 2).

239 The important simplification in the LGGE model is the replacement of geometry dependent
 240 parameters, not available for past conditions, with a variable γ , adjusted in order to obtain a
 241 continuous densification rate at the boundary between the first and the second stage of

242 densification.

243 A first modification in this module consists of extending the Alley (1987) scheme to the upper two
244 meters of the firn rather than using a constant density value. Indeed, since the model is not able to
245 represent the metamorphism of the first two meters, we impose a constant pressure of 0.1 Bar (see
246 Equation 6), which is an approximation of the pressure at 2-3 m depth. It results in a nearly constant
247 densification rate in the top 2-3 m rather than a constant density in the top 2 meters.

248 The second modification concerns the transition between the snow and firn densification stages at
249 the relative density of 0.6. In Equation (4), the term $\left(1 - \frac{5}{3} \times D_{rel}\right)$ implies that the densification
250 speed drops to zero at $D_{rel} = \frac{3}{5}$ (i.e. 0.6 the maximal compaction density). The second stage of
251 densification (firn densification) is driven by an important overburden pressure on the contact area
252 hence associated with a high densification speed. The transition between the sharp decrease of the
253 densification speed for D_{rel} values close to 0.6 in the snow densification stage and the high
254 densification speed at the beginning of the firn densification (i.e. in the same range of value for D_{rel})
255 causes some model instabilities especially at sites with high temperature and accumulation rate. In
256 order to improve the model stability, we go back to the definition of the term $\left(1 - \frac{5}{3} \times D_{rel}\right)$ in the
257 initial formulation of Alley (1987). This term relies on a correlation between the coordination
258 number (N) and relative density: $D_{rel} = 10 N$. We slightly modified this relationship and impose $D_{rel} =$
259 $10 N - 0.5$ which better matches the data on Figure 1 of Alley (1987). This results in replacing the
260 term $\left(1 - \frac{5}{3} \times D_{rel}\right)$ in Equation (4) with $\left(1 + \frac{0.5}{6} - \frac{5}{3} \times D_{rel}\right)$. This modification shifts the density at
261 which the densification rate becomes zero from 0.6 to 0.65 and suppresses the model instability.

262

263 We also examine the effect of temperature on the first-stage densification mechanism and on the
264 critical density. Alley (1987) calculated a viscosity (ν) related activation energy of 41 kJ/mol,
265 consistent with recommended values for grain-boundary diffusion (42 kJ/mol) or measured from
266 grain growth rate (Alley, 1987 and references therein). In Goujon et al. (2003), no explicit
267 temperature effect is used but the parameter γ varies by several orders of magnitude from site to
268 site. The parameter γ is calculated to maintain a continuous densification rate between the first and
269 second stages at a chosen critical density. We translate the variations from site to site of $\gamma = (2 \lambda R)$
270 $/ (15 \nu r^2)$, where λ is the bond thickness, R the grain radius, ν the bond viscosity and r the bond
271 radius (as in Equation 5), into $\gamma = \gamma' \exp(-Q/RT)$, and calculate the activation energy Q using a
272 classical logarithmic plot as a function of 1000/T (see e.g. Herron and Langway, 1980). We obtain a
273 value of 48 kJ/mol. Using the revised temperature dependency for the firn densification mechanism

274 (see next section), a slightly higher value of $Q = 49.5$ kJ/mol is calculated (Supplementary Figure S1).
 275 This is fairly similar to the values in Alley (1987) but much higher than the value in the upper firn of
 276 the Herron and Langway (1980) model: 10.16 kJ/mol. Incorporating this explicit temperature
 277 dependency term, we obtain our new final expression for the upper firn densification rate:

$$278 \frac{dD_{rel}}{dt} = \gamma' \left(\frac{\max(P, 0.1 \text{ bar})}{D_{rel}^2} \right) \left(1 + \frac{0.5}{6} - \frac{5}{3} \times D_{rel} \right) \times e^{\left(-\frac{Q}{RT} \right)} \quad (6)$$

280
 281 where $\gamma' \times e^{\left(-\frac{Q}{RT} \right)}$ is equivalent to γ in Equation (4). However γ varies by two orders of magnitude
 282 as a function of temperature whereas γ' remains in the range from 0.5×10^9 to 2×10^9 bar⁻¹.

283 Finally, the temperature dependency of the critical density, which defines the boundary between
 284 the first and second stage densification mechanisms, is also re-evaluated. According to Benson
 285 (1960) and Arnaud (1997; 2000), this critical density increases with temperature. However the slope
 286 change in density profiles associated with the critical density may be difficult to locate and the
 287 Benson (1960) and Arnaud (1997) parameterizations are based on only few observation sites. We
 288 evaluate the critical density values which allow the best match of density data by our model results
 289 at 22 sites and do not find any correlation between critical density and temperature or accumulation
 290 rate (Supplementary Figure S2). We thus remove this dependency with temperature included in the
 291 old version of the LGGE model and use a mean relative critical density of 0.56 at the boundary
 292 between the first and second stage of densification in the new version of the model. The effect of
 293 surface density was also tested and does not have a strong impact on the model results
 294 (Supplementary Figure S3).

295 296 2.2 Densification of firn

297
 298 At this stage, the observation of density profiles with depth suggests that the densification rate is
 299 controlled by a classical power law creep as used for ice deformation (Arzt et al., 1983; Maeno and
 300 Ebinuma, 1983; Wilkinson and Ashby, 1975). Arzt (1982) proposed a pressure sintering mechanism
 301 for firn densification following a power law creep and taking into account the progressive increase
 302 of the coordination number. He solved the geometrical problem of compressing a random dense
 303 packing of monosized spheres with associated deformation of each sphere into irregular polyhedra.
 304 Equation (23) of Arzt (1982) is directly used in the firn densification model.

305 306 2.2.1 Revised temperature sensitivity of the firn densification rate

307

308 A strong assumption in the firn densification module is the constant activation energy corresponding
309 to self-diffusion of ice (60 kJ/mol). This choice corresponds to a unique mechanism supposed to
310 drive densification. Densification is thus assumed to be driven by dislocation creep (Ebinuma and
311 Maeno, 1987) in which the associated mechanism is lattice diffusion or self-diffusion. At the grain
312 scale, we can describe the lattice diffusion processes associated with dislocation as diffusion within
313 the grain volume of a water molecule from a dislocation site in the ice lattice to the grain neck in
314 order to decrease the energy associated with grain boundaries (Blackford, 2007). Typically, an
315 activation energy of 60 to 75 kJ/mol is associated with this mechanism (Arthern et al., 2010; Barnes
316 et al., 1971; Pimienta and Duval, 1987; Ramseier, 1967 and references therein).

317

318 However, multiple studies have already shown that several (6 or more) mechanisms can act
319 together for firn or ceramic sintering (Ashby, 1974; Blackford, 2007; Maeno and Ebinuma, 1983;
320 Wilkinson and Ashby, 1975): lattice diffusion from dislocations, grain surfaces or grain boundaries;
321 vapor transport; surface and boundary diffusions. In order to properly take these different
322 mechanisms into account, different activation energies (one activation energy per mechanism)
323 should ideally be introduced in the firn densification model. Actually, it has been observed that, at
324 warm temperature, an activation energy significantly higher than 60 kJ/mol could be favoured (up
325 to 177 kJ/mol between -1 and -5°C [Jacka and Li, 1994]) in order to best fit density profiles with firn
326 densification models (Arthern et al., 2010; Barnes et al., 1971; Jacka and Li, 1994, Morgan, 1991).
327 This suggests that a mechanism different from lattice diffusion is dominant for grain compaction at
328 high temperature (i.e. higher than -10°C). At low temperature (-50°C), by analogy with ceramic
329 sintering, lattice diffusion from the surface of the grains and/or boundary diffusion from grain
330 boundaries should be favoured (Ashby, 1974). The activation energy for surface diffusion is
331 estimated to be in the range 14-38 kJ/mol (Jung et al., 2004; Nie et al., 2009).

332

333 Following these arguments and despite the lack of experimental constraints to test this assumption,
334 we propose a new heuristic parameterization of the activation energy in the LGGE firn densification
335 model which increases the firn densification rate at low temperatures. We have thus enabled
336 introduction of three adjusted activation energies as proposed in Table 1 and Figure 2. We have
337 replaced the creep parameter in Equation (3) by:

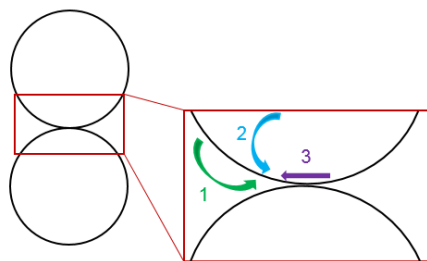
338

$$339 \quad A = A_0 \times \left(a_1 \times e^{\frac{-Q_1}{RT}} + a_2 \times e^{\frac{-Q_2}{RT}} + a_3 \times e^{\frac{-Q_3}{RT}} \right) \quad (7)$$

340

341 We have chosen a minimal number of mechanisms (3) for simplicity in the following but the
342 conclusions of our work would not be affected by a choice of more mechanisms.

343



344

345

346 *Figure 2: Different sintering mechanisms of snow for different temperatures proposed by analogy with the*
347 *hot ceramic sintering (inspired by Figure 1 in Ashby, 1974). Note that more sintering mechanisms can be found*
348 *in the literature: in its initial figure, Ashby (1974) mentioned 6 different mechanisms but only 2 permit*
349 *densification (lattice diffusion and boundary diffusion from grain boundary). The attributions of 3 different*
350 *mechanisms for the firn densification model based on the powder aggregate study from Ashby (1974) is only*
351 *a working hypothesis here.*

352

353 When building the new parameterization of the activation energy (Equation 7), the determination
354 of Q_1 , Q_2 and Q_3 on the one side and a_1 , a_2 and a_3 on the other side are not independent from each
355 other. We first determine three temperature ranges corresponding to the dominant mechanisms,
356 then we attribute values to the activation energies Q_1 , Q_2 and Q_3 . The coefficients a_1 , a_2 and a_3 are
357 finally adjusted to produce the expected evolution of the creep parameter with temperature, to
358 best reproduce $\delta^{15}\text{N}$ evolution over deglaciations (Section 3.2) and respect the firn density profiles
359 available (Section 3.1).

360 Hundreds of sensitivity tests have been performed imposing 3 activation energies at 3 different
361 typical temperatures, T_i . The initial values for Q_i are chosen as explained above (high value for Q_1
362 [Jacka and Li, 1994], classical value between 60 and 70 kJ/mol for Q_2 and low value for Q_3 to increase
363 the densification rate at low temperature). The initial values for a_i are derived through $a_i \cdot \exp(-Q_i/RT_i) = a_0 \cdot \exp(-60000/RT_i)$ and variations around the initial values of Q_i and a_i are randomly
364 generated. Only the values leading to realistic densification speed are kept and we found the
365 optimal tuning through reduction of the mismatch between model and data especially for the
366 deglacial amplitude of $\delta^{15}\text{N}$ in Dome C and Vostok. The constraint of keeping a correct agreement
367 of model results with present day density profiles and for the last deglaciation at warm sites strongly
368

369 reduces the possible choices of a_i and Q_i (Section 3). The best value obtained for Q_3 is lower than
 370 published values for surface or boundary diffusion but is necessary to reproduce the deglaciation at
 371 cold East Antarctic Sites. Sensitivity test C will illustrate the effect of using a higher value.

372

373 The resulting expression for the creep parameter A (Equation 7), does not strongly differ from using
 374 simply $A = A_0 \times e\left(-\frac{60000}{RT}\right)$, as used in the original model. To illustrate this point, we calculated an
 375 equivalent activation energy, Q_{eq} , such that $A = A_0 \times e\left(-\frac{Q_{eq}(T)}{RT}\right)$, and found Q_{eq} varying between
 376 54 and 61 kJ/mol (Supplementary Figure S4). Thus only moderate changes to the densification
 377 equation are needed to improve the behaviour of the model at cold temperature. In addition, only
 378 moderate changes in Q_{eq} are allowed to preserve the consistency between model results and
 379 present-day density profiles.

380

Activation Energy (J/mol)	Coefficient
$Q_1= 110000$	$a_1= 1.05*10^9$
$Q_2= 75000$	$a_2= 1400$
$Q_3= 1500$	$a_3= 6.0*10^{-15}$

381

382 *Table 1: Preferred set of values for the three activation energies and associated pre-exponential constants*

383

384 2.2.2 Sensitivity of the firm densification rate to impurities

385

386 Firm densification can be influenced by impurity content in snow. Alley (1987) already suggested
 387 that grain growth is influenced by impurities dissolved in ice, and that impurities in the grain
 388 boundaries affect the relative movement of snow grains. More recently, Hörhold et al. (2012)
 389 observed a correlation between the small scale variability of density and calcium concentration in
 390 Greenland and Antarctic firn cores. Based on this observation, Freitag et al. (2013) proposed that
 391 the densification rate depends on the impurity content. They implemented an impurity
 392 parameterization in two widely used densification models (Herron and Langway, 1980; Barnola et
 393 al., 1991), and were able to reproduce the density variability in two firn cores from Greenland and
 394 Antarctica.

395

396 We have implemented this parameterization in our model with the simple assumption that the
 397 impurity effect is the same for all mechanisms. It allows us to keep the number of tunable

398 parameters to a minimum, even though this assumption is probably not correct for the vapor
399 diffusion process. Note however that this will not affect the applications discussed below since
400 vapor diffusion is only important for warm sites. Concretely, we start again from the evolution of
401 the creep parameter with respect to temperature given in Equation (7) and add a dependency to
402 calcium concentration such as:

403

$$404 \text{ if } [Ca^{2+}] > [Ca^{2+}]_{crit} : Q' = f_1 \times \left[1 - \beta \ln \left(\frac{[Ca^{2+}]}{[Ca^{2+}]_{crit}} \right) \right] \times Q \quad (8)$$

$$405 \text{ if } [Ca^{2+}] < [Ca^{2+}]_{crit} : Q' = f_1 \times Q \quad (9)$$

406

407 With, $[Ca^{2+}]_{crit} = 0.5$ ng/g (the detection limit of continuous flow analysis). Q' represents the new
408 activation energy calculated as a function of the calcium concentration for each site. Our main
409 simulations are performed with the f_1 and β calculated by Freitag et al. (2013) for application within
410 the Herron and Langway model: $f_1 = 1.025$, $\beta = 0.01$. Using the values for application within the
411 Pimienta-Barnola model ($f_1 = 1.015$, $\beta = 0.0105$) leads to similar results (Section 3.2). For a first
412 evaluation of the impurity effect in our model, both the temperature and impurity effects are
413 combined through the application of Equations (8) and (9) to each of the three different activation
414 energies Q_1 , Q_2 and Q_3 . We use raw data of the calcium concentration for all the sites when available
415 even if question may arise on calcium concentration being the best diagnostic for dust content.

416 The values of a_i and Q_i were not readjusted after the implementation of impurity effects to avoid
417 adding tuning parameters. Still, because the large range of calcium concentrations encountered in
418 past climate conditions has a strong impact on model results, this may be a solution to reduce the
419 model-data mismatch. This is explored in Section 3 through a sensitivity test D. In the same section,
420 we will also propose a modification of the Freitag parameterization using thresholds to reduce the
421 model-data mismatch.

422

423 2.3 Densification of ice

424

425 As in Goujon et al. (2003), the final densification stage begins at the close-off density derived from
426 air content measurements in mature ice. Further porosity reduction results in an air pressure
427 increase in the bubbles (Martinerie et al., 1992, Appendix 1). This density is calculated using the
428 temperature dependent close-off pore volume given by Martinerie et al. (1994). Further
429 densification of this bubbly ice is driven by the pressure difference between ice matrix and the air
430 in bubbles (Maeno and Ebinuma, 1983; Pimienta, 1987). The densification rate strongly decreases

431 with depth as these two opposite pressures tend to balance each other (Goujon et al., 2003). This
432 stage is not essential for this study since $\delta^{15}\text{N}$ entrapped in air bubbles does not evolve anymore.

433

434 2.4 Lock-in depth

435

436 In the previous version of the model, the LID was computed as a fixed closed to total porosity ratio.
437 The ratio value used has been adjusted for each drilling site, for example it is 21% for Vostok and
438 13% at Summit in Goujon et al. (2003), but it was time independent and thus insensitive to climate.
439 We revised the LID definition in order to relate its present day geographic variations to climatic
440 parameters.

441

442 Ideally, $\delta^{15}\text{N}$ profiles in the open porosity of the firn follow the barometric slope in the diffusive
443 zone, and show no variations in the lock-in zone. However $\delta^{15}\text{N}$ data can deviate from this
444 behaviour, especially at the very low accumulation rate sites such as Dome C, Vostok or Dome Fuji,
445 where no $\delta^{15}\text{N}$ plateau is observed in the lock-in zone (Bender et al., 1994; Kawamura et al., 2006;
446 Landais et al., 2006). Moreover, as we aim at comparing our model results with $\delta^{15}\text{N}$ data in deep
447 ice cores, the most consistent LID definition should refer to $\delta^{15}\text{N}$ data in mature ice but very few
448 measurements are available for recent ice. Systematic $\delta^{15}\text{N}$ measurements in the closed porosity of
449 the deep firn or recently formed mature ice would be very helpful to better constrain the LID in the
450 future. We take advantage of recent advances in gas transport modelling (Wittrant et al., 2012) that
451 allowed correct simulation of the $\delta^{15}\text{N}$ behaviour in deep firn. Observations of modern firn air
452 profiles show that the thickness of the lock-in zone (the zone in the deep firn with constant $\delta^{15}\text{N}$)
453 increases when the snow accumulation rate increases (Wittrant et al., 2012). We estimate $\delta^{15}\text{N}$ in
454 ice, i.e. after complete bubble closure, at 12 firn air pumping sites with the Wittrant et al. (2012)
455 model. For each site, the lock-in density (ρ_{LI}) is then defined as the density at which the modelled
456 $\delta^{15}\text{N}$ value in the open porosity of the firn equals the modelled $\delta^{15}\text{N}$ in ice. The resulting lock-in
457 density is strongly related to the accumulation rate (Supplementary Figure S5). As a result, we
458 parameterized the lock-in density (ρ_{LI}) as a function of the accumulation rate, following:

459

$$460 \rho_{\text{LI}} = 1.43 \times 10^{-2} \times \ln(1/A_c) + 0.783 \quad (10)$$

461

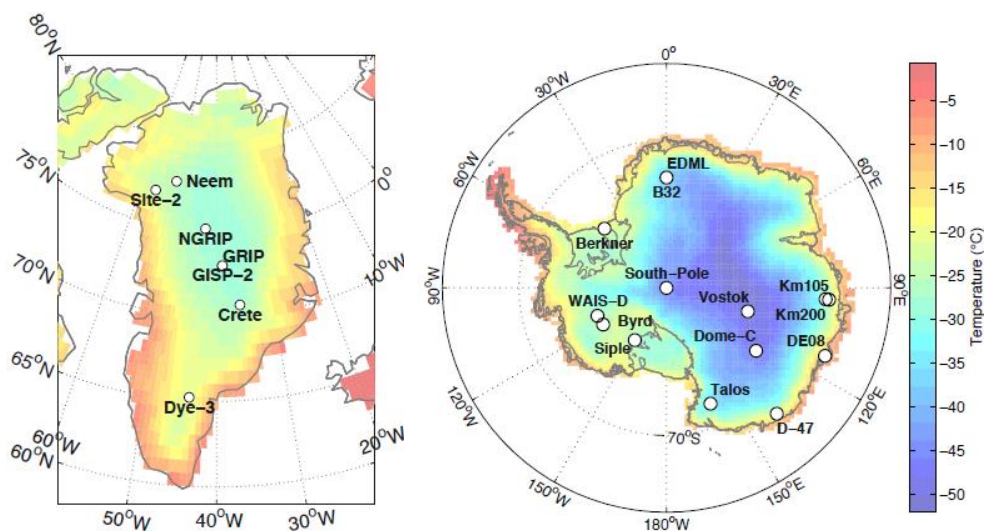
462 This parameterization leads to ρ_{LI} variations in the range 780-840 kg/m^3 (Supplementary Figure S5)
463 and a much better agreement between the modelled LID and $\delta^{15}\text{N}$ measured in firn samples at

464 available sites than when using a fixed closed / total porosity ratio. However, when used for
465 simulating the LID during glacial periods with extremely low accumulation rate, it can predict a lock-
466 in density that is higher than the close-off density, which is unrealistic. We thus also added a
467 threshold in our new definition of the lock-in density: when ρ_{LI} exceeds the close-off density (ρ_{CO} ,
468 Section 2.3), we impose ρ_{LI} to be equal to ρ_{CO} .

469

470 3. Results

471



472

473

474 *Figure 3: Maps of Greenland and Antarctica showing field sites and mean annual temperature from ERA*
475 *interim (Dee et al., 2011)*

476

477 3.1 Firn density profiles

478 We assessed the behaviour of the model by comparing measured and modelled firn density profiles
479 from 22 sites from Greenland and Antarctica (Figure 3). Figure 4 shows this comparison at Byrd,
480 NEEM, Dome C and Vostok, and other sites are displayed in the supplement (Supplementary Figure
481 S6). A polynomial fit was adjusted to the density data in order to facilitate the comparison with
482 model results. The data dispersion around the fit can be due natural density variations and/or
483 measurement uncertainties.

484

485 A comparison of snow density measurement methodologies concluded that uncertainties are about
486 10 % (Proksch et al., 2016). Moreover, although firn density profiles are often used, the
487 measurement technique is not always well documented. Efforts were made in this study to mention
488 the methodology when available (Supplementary Table S1). At high densities (below bubble closure

489 depth), the hydrostatic weighing technique is expected to be about 10 times more precise than
490 simple volume and mass measurements (Gow, 1968) but rarely used, although it is important to
491 correctly evaluate the fairly small density difference with pure ice density. We should note that the
492 agreement between our model results and data is good at high densities for the three sites where
493 hydrostatic weighing technique was used: Site 2 and D-47 (Supplementary Figure S6) as well as Byrd
494 (Figure 4).

495

496 High-resolution measurements on small samples often aim at documenting the natural variability
497 of density. Our model only simulates bulk density, and to illustrate a meaningful comparison, the
498 highest resolution data (at DE08, B29, B32 and Dome C) were averaged over 0.25 m windows before
499 being plotted. At some sites, a similar averaging was already performed before data publication (e.g.
500 1 m averaging at Byrd and Site 2, 0.5 m averaging at Mizuho). At a large number of sites, especially
501 deep ice core drilling sites, measurements were performed on large volume samples. Still, it should
502 be noted that at NEEM, although large volume samples were used, the data dispersion is higher
503 than for Byrd (Figure 4) and part of the discrepancy between the model and data may be due to the
504 uncertainty in the data.

505

506 For our study we have gathered density data covering the whole firn depth range, for which we had
507 confidence in the data quality and the major site characteristics (temperature, accumulation).
508 Although the effects of uncertainties on the data and natural density variability cannot be
509 completely separated, we evaluate the data dispersion around the polynomial fit:

510

$$511 \quad \sigma_{fit-data} = \sqrt{\left[\frac{\sum_{i=1}^{N_{max}} (\rho_{fit}^i - \rho_{measured}^i)^2}{N_{max}} \right]} \quad (11)$$

512

513 where N_{max} is the number of steps of data points, ρ_{fit} represents the regression of the density profile
514 and $\rho_{measured}$ the measured density averaged on a 0.25 m window. $\sigma_{fit-data}$ generally lies below 10.0
515 kg/m^3 (Figure 5).

516 In order to visualize the model data comparison with the different versions of the model on the 22
517 selected sites, we calculate the following deviation in parallel to the $\sigma_{fit-data}$ above (Equation 11):

518

$$\sigma_{model-fit} = \sqrt{\left[\sum_{i=1}^{N_{max}} \frac{(\rho_{model}^i - \rho_{fit}^i)^2}{N_{max}} \right]} \quad (12)$$

520

521 Note that we compare here the model to the fit of the data and not directly to data because of the
 522 strong site to site differences in the data (e.g. data resolution, sample size). Figure 5 and
 523 Supplementary Table S1 display the $\sigma_{model-fit}$ for the 22 different sites before and after modifications
 524 detailed in Section 2.

525

526 3.1.1. Data – model comparisons using the old model

527

528 Comparing our model results to density data is not trivial due to the diversity in measurement
 529 techniques and samplings discussed above, as well as the natural variability in density that we do
 530 not capture with a simplified model aiming at simulating very long time scales. A rough indication is
 531 given by comparing $\sigma_{model-fit}$ and $\sigma_{fit-data}$. They are of the same order of magnitude although $\sigma_{fit-data}$ is
 532 always lower than $\sigma_{model-fit}$ (Figure 5), confirming that the old model is likely not able to fully
 533 represent the diversity of the density profiles at the 22 measurement sites.

534 The model-data agreement is variable among the different sites even for those with similar surface
 535 climatic conditions. The temperatures and accumulation rates at Dome C and Vostok being similar,
 536 model results at these sites are similar, but the density data have a clearly different shape. At
 537 Vostok, a high densification rate is observed well above the critical density of about 550 kg/m³. One
 538 possible reason is the very different flow regimes of the two sites, one being at a Dome summit, and
 539 the other on a flow line and subject to a horizontal tension (Lipenkov et al., 1989). This is not taken
 540 into account in our simplified 1D model. Some density data at other sites also show no densification
 541 rate change near the critical density, resulting in model-data mismatches (see Siple Dome, km 105,
 542 km 200, Mizuho on Supplementary Figure S6).

543 The main disagreement between the old model and data is observed at the transition between the
 544 first and the second densification stage with too high modeled densities and an associated slope
 545 change in the density profile that is too strongly imprinted. This effect is due to a densification rate
 546 that is too high in the first stage.

547

548 3.1.2. Data – model comparisons using the new model with only one activation energy

549

550 The modifications of the first densification stage described in Section 2.1 mainly reduce the slope

551 change at the transition between the Alley (1987) and Arzt (1982) mechanisms (not shown). It also
552 suppresses an instability of the previous model version which could fail to find a continuous
553 densification rate at the boundary between Alley (1987) and Arzt (1982) mechanisms.

554 However the new model still shows a tendency to overestimate the snow densification rate and
555 then underestimate the densification rate in the firn, as shown for NEEM and Vostok on Figure 4.

556 Still, looking at all different firn profiles, the general agreement between modeled and measured
557 firn density profiles is preserved. The agreement between measured and modeled firn density is
558 increased for some sites at (1) low accumulation rate and temperature in Antarctica (Dome A,
559 Vostok and Dome C but not South Pole) and at (2) relatively high temperature and accumulation
560 rate (Dye 3, Siple Dome, NEEM). In parallel, a larger disagreement between model and data is
561 observed for some other sites particularly in coastal Antarctica (DE08, Km 200, WAIS Divide). When
562 introducing these modifications for simulating $\delta^{15}\text{N}$ evolutions over the last deglaciation, no
563 significant changes are observed with respect to simulations run with the old LGGE model. This is
564 not unexpected since most of the modifications concern the first stage of densification (top 10-15
565 m of the firn). The other modification concerns the LID definition, it only has a small impact on the
566 model results for the glacial-interglacial transitions and slightly increases the model – data mismatch
567 over deglaciations (Supplementary Figure S7).

568

569 3.1.3. Data-model comparisons using the new model with three activation energy and
570 implementation of impurity effect

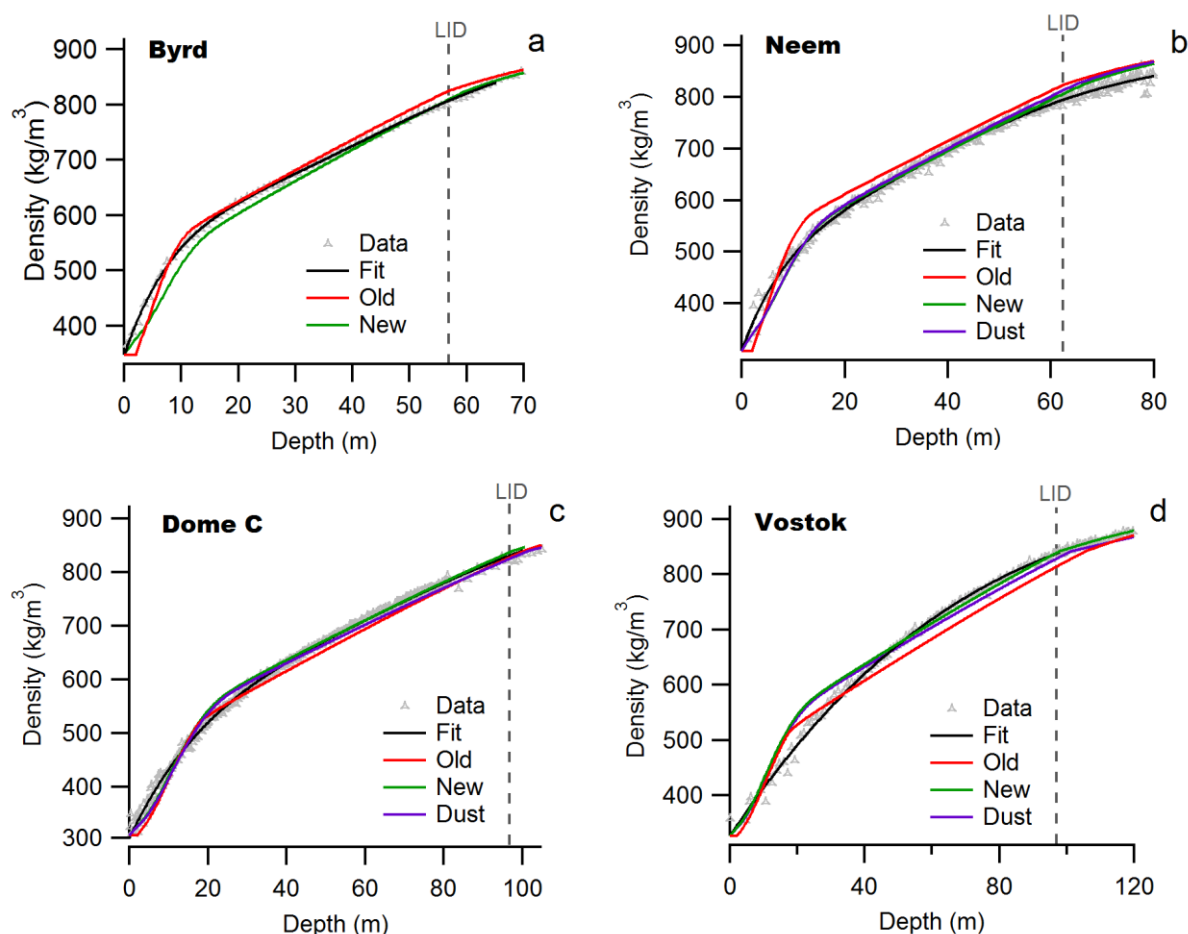
571

572 The introduction of three different activation energies for different temperature ranges leads to
573 changes of the modeled density profiles at high densities (above about 800 kg/m^3). A clear
574 improvement is obtained for example at South Pole (Supplementary Figure S6), although the overall
575 impact of using three activation energies remains small.

576 The incorporation of the impurity effect following the Freitag et al. (2013) parameterization in our
577 model slightly deteriorates the model-data agreement because no specific re-adjustment of model
578 parameters was performed. However the model prediction of the density profiles remains correct
579 although the impurity effect parameterization was developed for a different purpose, i.e.,
580 simulating density layering (Freitag et al., 2013). This encouraged us to test this simple
581 parameterization in glacial climate conditions.

582

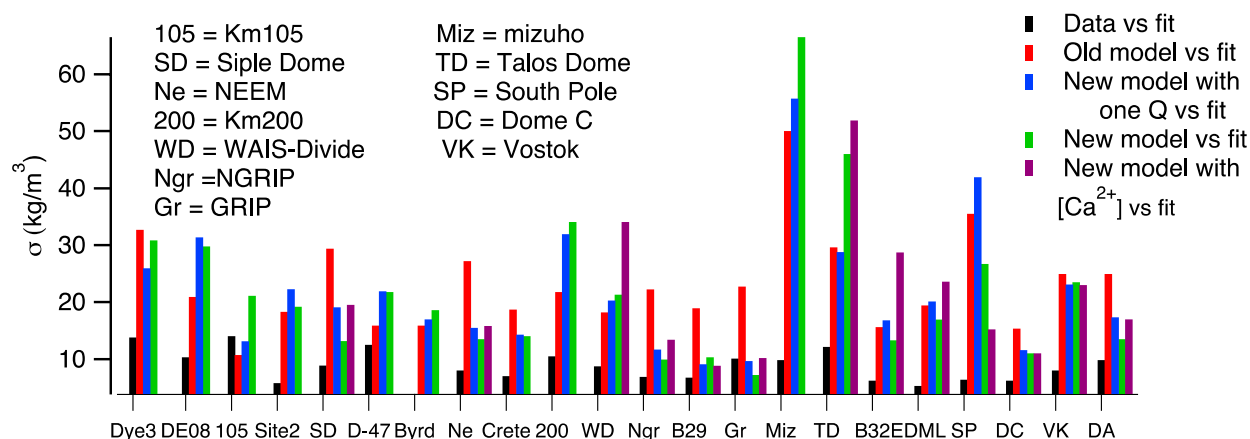
583 Overall, $\sigma_{\text{model-fit}}$ is only improved by 3% when using the modified model (3 activation energies and
 584 implementation of impurity effect) instead of the former Goujon et al. (2003) mechanical scheme.
 585 We thus conclude that the two versions of the model perform equally well.



586
 587
 588 *Figure 4: Density profiles of Byrd (a), NEEM (b), Dome C (c) and Vostok (d). The grey triangles correspond to the data.*
 589 *The black line corresponds to the polynomial fit, the red one to the old simulation, the green one to the new simulation*
 590 *and the purple one to the new simulation with impurity effect.*

591
 592 Finally, it should be noted that our main purpose is to improve the agreement between the
 593 modelled LID and the evolution of $\delta^{15}\text{N}$ over deglaciations in Antarctica. Thus, in addition to the
 594 above comparison of density profiles, we compared the depths at which the LID density, as defined
 595 by Equation (10), is reached in the polynomial fit to the data and in the new model results. In the
 596 old version of the model, the LID differences between the model and data range between -17.9 m
 597 (at South Pole) and +8.6 m (at km 200) with a small mean value of -1.9 m and a standard deviation
 598 of 6 m. In the new version, the LID differences between the model and data are comparable, ranging
 599 between -14.1 m (at South Pole) and +12.8 m (at Talos Dome) with a small mean value of -0.7 m and
 600 a standard deviation of 6 m. Similar results are obtained for Δage (see Supplementary Table S2): the

601 agreement with the data is similar for all model versions, and most cold sites are improved with the
 602 new model. However the $\sigma_{\text{model-fit}}$ values remain high compared to the variability of the data ($\sigma_{\text{fit-data}}$,
 603 black bars in Figure 5). We thus conclude from this section that the LGGE new firn densification
 604 model preserves the good agreement between (1) modelled and measured firn density profiles and
 605 (2) modelled and measured LID. We explore in the next section the performances of the new model
 606 for coldest and driest conditions by looking at the modelled LID and hence $\delta^{15}\text{N}$ evolution over
 607 glacial – interglacial transitions.
 608



609
 610 *Figure 5: Representation of the $\sigma_{\text{fit-data}}$ in black and the $\sigma_{\text{model-fit}}$ (in red for the old model, in blue for the model
 611 with the new parameterization except the three activation energies, in green for the new model with three
 612 activation energy and in purple for the new model with the impurity effect) at 22 Greenland and Antarctic
 613 sites. The site characteristics are provided in Supplementary Table S1.*

614
 615 3.2 $\delta^{15}\text{N}$ glacial-interglacial profiles

616
 617 In order to test the validity of the densification model in a transient mode, we model the time
 618 evolution of $\delta^{15}\text{N}$ over the last deglaciation, and compare it to measurements at 4 Antarctic and
 619 Greenland deep ice-core sites: Dome C (cold and low accumulation site in Antarctica with a strong
 620 mismatch observed between data and the old model), EDML (intermediate temperature and
 621 accumulation rate in Antarctica with a significant mismatch between data and the old model), WAIS-
 622 Divide (high temperature and accumulation rate site in Antarctica with a good model-data
 623 agreement) and NGRIP (Greenland site with a good agreement between model and data) (Figure 3).
 624 The computation of $\delta^{15}\text{N}$ depends on the convective zone thickness, the LID and on the firn
 625 temperature profile. The gravitational $\delta^{15}\text{N}$ signal is indeed calculated from the LID and mean firn

626 temperature according to the barometric equation (Equation 1). The thermal $\delta^{15}\text{N}$ depends on the
627 temperature gradient between the surface and the LID. A small thermal signal exists in Antarctica
628 because of geothermal heat flux (with an average change of about 0.02 ‰ during deglaciation) but
629 no millennial variations are expected because the temperature variations are slow ($<2^\circ\text{C}/1000$
630 years) compared to abrupt climate changes observed in Greenland (e.g. NGRIP).
631 The model calculates for each ice core depth the firn diffusive column height and thermal
632 fractionation at the bottom of the firn. To take into account the smoothing due to gas diffusion in
633 the open pores and progressive bubble close-off (Schwander et al., 1993), we smooth the $\delta^{15}\text{N}$
634 output with a log-normal distribution, of width $\Delta\text{age}/5$ and $\text{sigma}=1$ (Köhler et al., 2011; Orsi et al.,
635 2014). This formulation of the smoothing takes into account the variations of the gas-age
636 distribution with time. Note that it has been suggested that the width in Köhler et al. (2011) is too
637 wide (<http://www.clim-past.net/7/473/2011/cp-7-473-2011-discussion.html>). Still, using a smaller
638 width does not modify the modelled amplitude of the $\delta^{15}\text{N}$ signal over the deglaciation so that our
639 conclusions are not affected by such uncertainty.

640

641 3.2.1 Input scenarios

642

643 For the simulation of the $\delta^{15}\text{N}$ evolution over the last deglaciation, the firn densification model is
644 forced by a scenario of surface temperature and accumulation rate deduced from ice core data
645 (Supplementary Table S3). In Greenland (NGRIP, GISP2), the temperature is reconstructed using the
646 $\delta^{18}\text{O}_{\text{ice}}$ profiles together with indication from borehole temperature measurements (Dahl-Jensen,
647 1998) and $\delta^{15}\text{N}$ data for NGRIP (Kindler et al., 2014) for the quantitative amplitude of abrupt
648 temperature changes. Greenland accumulation rate is deduced from layer counting over the last
649 deglaciation (e.g. Rasmussen et al., 2006). The uncertainty in the temperature reconstructions can
650 be estimated to $\pm 3^\circ\text{C}$ over the last deglaciation in Greenland (Buizert et al., 2014). As for the
651 Greenland accumulation rate, an uncertainty of 20% can be associated with the LGM value (Cuffey
652 and Clow, 1997; Guillevic et al., 2013; Kapsner et al., 1995). In Antarctica, both temperature and
653 accumulation rate are deduced from water isotopic records except for WAIS-Divide, where layer
654 counting back to the last glacial period is possible (Buizert et al., 2015). Temperature uncertainty for
655 the amplitude of the last deglaciation is estimated to -10% to +30% in Antarctica (Jouzel, 2003). The
656 reason for such asymmetry is mainly linked to outputs of atmospheric general circulation models
657 equipped with water isotopes. These models suggest that the present day spatial slope between
658 $\delta^{18}\text{O}$ and temperature most probably underestimates the amplitude of the temperature change

659 between glacial and interglacial period. We have used this estimate of asymmetric uncertainty on
660 the amplitude of temperature change during deglaciation in our study. Recent studies have also
661 suggested that the relationships between water isotopes and temperature and between water
662 isotopes and accumulation rate can be applied with confidence in Antarctica for glacial temperature
663 reconstruction (Cauquoin et al., 2015) while one should be cautious for interglacial temperature
664 reconstruction with warmer conditions than today (Sime et al., 2009). Finally, a recent estimate of
665 the deglacial temperature increase based on $\delta^{15}\text{N}$ measurements at WAIS (Cuffey et al., 2016) led
666 to a 11.3°C temperature increase over the last deglaciation (1°C warming to be attributed to change
667 in elevation). This is larger than the temperature increase reconstructed in East Antarctica from
668 water isotopes by 2-4°C and again not in favour of a “warm” LGM.

669 In the construction of the AICC2012 chronology (Bazin et al., 2013; Veres et al., 2013), the first order
670 estimate of accumulation rate from water isotopes for EDML, Talos Dome, Vostok and Dome C has
671 been modified by incorporating dating constraints or stratigraphic tie points between ice cores
672 (Bazin et al., 2013; Veres et al., 2013). The modification of the accumulation rate profiles over the
673 last deglaciation for these 4 sites is less than 20% and the uncertainty of accumulation rate
674 generated by the DATICE model used to build AICC 2012 from background errors (thinning history,
675 accumulation rate, LID) and chronological constraints is 30% for the LGM (Bazin et al., 2013; Frieler
676 et al., 2015; Veres et al., 2013). Still, it should be noted that the uncertainty of 20% on LGM
677 accumulation rate on central sites as given in the AICC2012 construction is probably overestimated.
678 Indeed, deglaciation occurs around 500 m depth at Dome C, hence with small uncertainty on the
679 thinning function and on the accumulation rate. These values are consistent with previous estimates
680 of accumulation rate uncertainties over the last deglaciation ($\pm 10\%$ for Dome C (Parrenin et al.,
681 2007) and $\pm 30\%$ in EDML (Loulergue et al., 2007)).

682
683 We showed in Section 2.1 that surface density does not have a strong impact on the LID
684 determination (Supplementary Figure S3). We do not have any indication of surface density in the
685 past, so we impose a constant surface density of 0.35 for all sites at all times for transient runs. In
686 order to convert the LID (deduced from density) to the diffusive column height measured by $\delta^{15}\text{N}$,
687 we need an estimate of the convective zone in the past. We use a 2 m convective zone for all sites,
688 except Vostok, where we use 13 m, in accordance with firn measurements (Bender et al., 2006). We
689 assume that the convective zone did not evolve during the last deglaciation, consistently with dating
690 constraints at Dome C and at Vostok during Termination 2 (Parrenin et al., 2012; Bazin et al., 2013;
691 Veres et al., 2013; Landais et al., 2013).

692

693 3.2.2 Transient run with the old model

694

695 In this section, we focus on the $\delta^{15}\text{N}$ evolution over the deglaciation at different Greenland and
696 Antarctic sites as obtained from the data and as modelled with the old version of the LGGE model.
697 This comparison serves as a prerequisite for the comparison with outputs of the revised model over
698 the same period for the same polar sites. The comparison between the old LGGE model and $\delta^{15}\text{N}$
699 data over the last deglaciation shows the same patterns already discussed in Capron et al. (2013).
700 At Greenland sites, there is an excellent agreement between model and data showing both the
701 decrease in the mean $\delta^{15}\text{N}$ level between the LGM and the Holocene and the $\sim 0.1\text{‰}$ peaks in $\delta^{15}\text{N}$
702 associated with the abrupt temperature changes (end of the Younger Dryas, Bølling-Allerød,
703 Dansgaard-Oeschger 2, 3 and 4, Figure 6 and Supplementary Figure S8). On the other hand, the
704 modelled and measured $\delta^{15}\text{N}$ over the last deglaciation show significant dissimilarities in Antarctic
705 $\delta^{15}\text{N}$ profiles displayed on Figure 6 and Supplementary Figure S8, except at the relatively high
706 accumulation rate and temperature site of WAIS-Divide where the model simulates properly the
707 $\delta^{15}\text{N}$ evolution in response to the change in accumulation and mean firn temperature estimated
708 from water isotopic records and borehole temperature constraints (Buizert et al., 2015). Note that
709 in Buizert et al. (2015), the modelled $\delta^{15}\text{N}$ was obtained from the Herron and Langway model. For
710 the other Antarctic sites (Figure 6), we observe that model and data disagree on the $\delta^{15}\text{N}$ difference
711 between the LGM and Holocene levels. At EDML, Dome C and Vostok, the model predicts a larger
712 LID during the LGM, while $\delta^{15}\text{N}$ suggests a smaller LID compared to the Holocene (with the
713 assumption of no change in convective zone during the deglaciation). In addition, the measured
714 $\delta^{15}\text{N}$ profiles at Berkner Island, Dome C, EDML and Talos Dome display an additional short term
715 variability, i.e. $\delta^{15}\text{N}$ variations of 0.05‰ in a few centuries during stable climatic periods. These
716 variations can be explained by the ice quality (coexistence of bubbles and clathrates) at Dome C and
717 EDML. Indeed, for pure clathrate ice from these two sites, such short term variability is not observed
718 (e.g. Termination 2 at Dome C, Landais et al., 2013). At Berkner Island and Talos Dome, these
719 variations cannot be explained by the quality of the measurements, by thermal effects nor by dust
720 influence. They are also not present in the accumulation rate and temperature forcing scenarios
721 deduced from water isotopes (Capron et al., 2013). In the absence of alternative explanations, we
722 can thus question the existence and variations of a convective zone and/or the accuracy of the
723 reconstruction of past accumulation rate and temperature scenarios from water isotopes in
724 Antarctica except at WAIS-Divide where layer counting is possible over the last deglaciation. We

725 thus explore further the influence of accumulation rate and temperature uncertainties on the $\delta^{15}\text{N}$
726 modelling.

727

728 The uncertainties in the changes of temperature and accumulation rates over the deglaciation
729 significantly influences the simulated $\delta^{15}\text{N}$, as already shown in previous studies and this sensitivity
730 of $\delta^{15}\text{N}$ has even been used to adjust temperature and/or accumulation rate scenarios (Buizert et
731 al., 2013; Guillevic et al., 2013; Kindler et al., 2014; Landais et al., 2006). We tested the influence of
732 the accumulation rate and temperature scenarios on the simulated $\delta^{15}\text{N}$ profiles for the last
733 deglaciation, but even with large uncertainties in the input scenarios, it is not possible to reproduce
734 the measured Antarctic $\delta^{15}\text{N}$ increase at Dome C and EDML with the old version of the LGGE model.

735

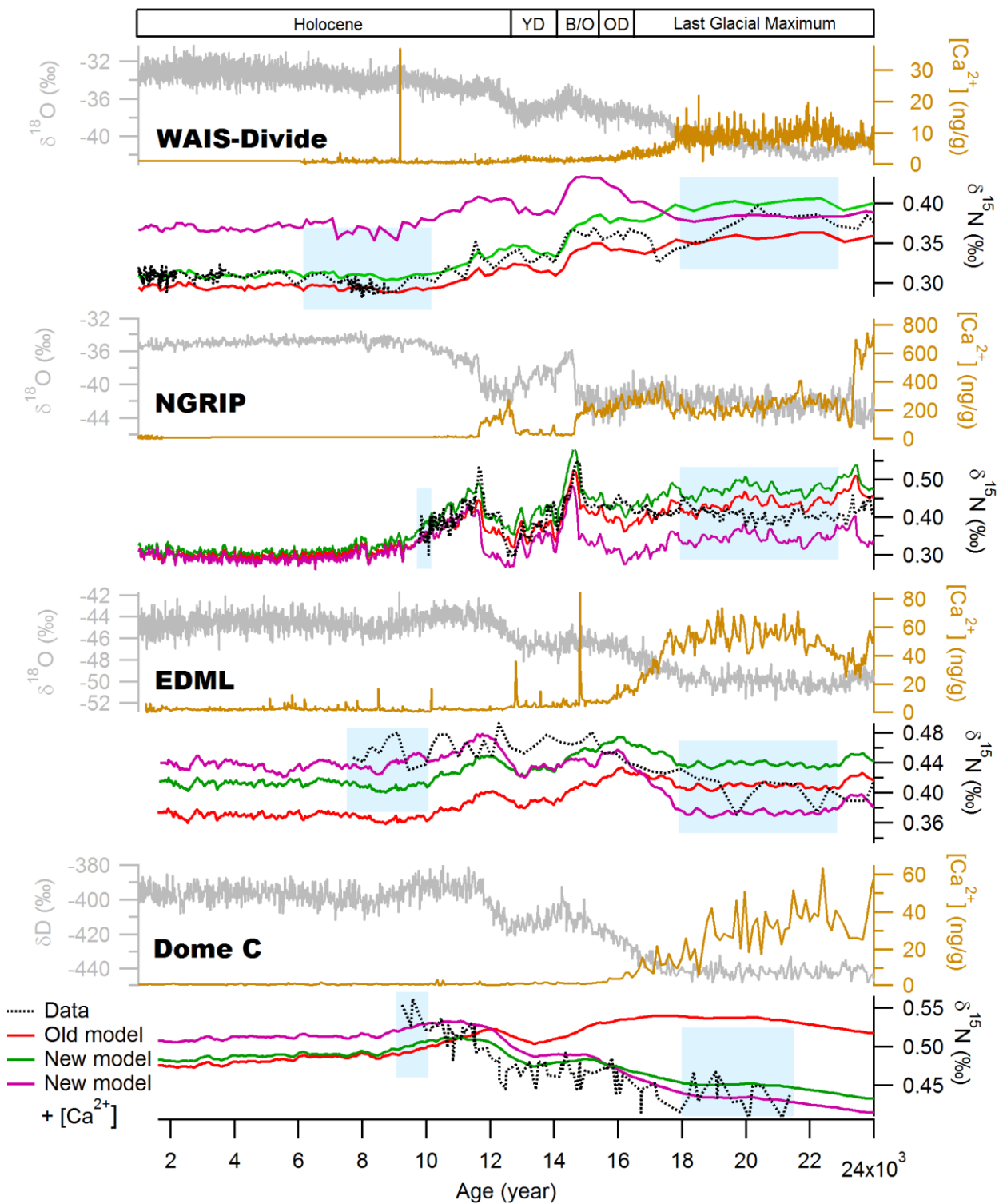
736 This result is illustrated on Figure 7 where we display a comparison between the amplitude of the
737 measured $\delta^{15}\text{N}$ change and the amplitude of the modelled $\delta^{15}\text{N}$ change with the Goujon version
738 over the last deglaciation. For this comparison, we calculated the Last Glacial Maximum (LGM) $\delta^{15}\text{N}$
739 average over the period 18-23 ka and the Early Holocene (EH) $\delta^{15}\text{N}$ average over the period 6-10 ka
740 (or smaller, depending on available data, cf blue boxes on Figure 6). We estimated the uncertainty
741 in the measured $\delta^{15}\text{N}$ change by calculating first the standard deviation of the $\delta^{15}\text{N}$ data over each
742 of the two periods, LGM and EH as $\sigma_{15\text{N_data_EH}}$ and $\sigma_{15\text{N_data_LGM}}$ and then the resulting uncertainty

743 in the $\delta^{15}\text{N}$ change as: $\sigma_{15\text{N_EH-LGM}} = \sqrt{\sigma_{15\text{N_data_EH}}^2 + \sigma_{15\text{N_data_LGM}}^2}$

744

745 As for the modelled $\delta^{15}\text{N}$ change, associated error bars are deduced from the uncertainty in the
746 temperature and accumulation input scenarios (shown on Supplementary Figure S9 for the
747 improved model). The total error bar hence shows the difference between most extreme
748 accumulation rate or temperature input scenarios. In these sensitivity tests, we assumed that it is
749 not possible to have an underestimation of the temperature change while at the same time have an
750 overestimation of the accumulation rate (or the opposite) because changes in accumulation rate
751 and temperature are linked, at least qualitatively when comparing LGM and Holocene mean values.

752



753

754

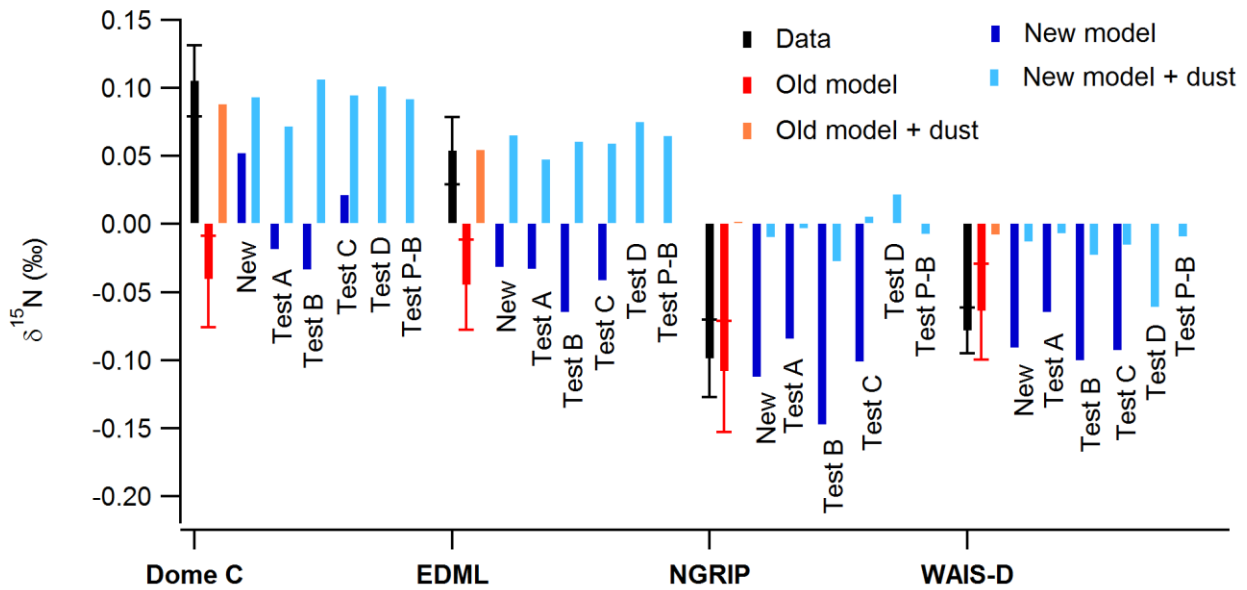
755

756

757

758

Figure 6: Comparison of the measured $\delta^{18}\text{O}$ or δD (grey), the calcium concentration (gold), the measured $\delta^{15}\text{N}$ (black) and the modelled $\delta^{15}\text{N}$ (old (red), new version (green) and new version with impurity (purple)) of the LGGE model for WAIS-Divide, NGRIP, EDML and Dome C. Blue boxes for each sites indicate the periods over which the $\delta^{15}\text{N}$ average for the LGM and EH have been estimated for the calculation of the amplitude of the $\delta^{15}\text{N}$ change over the deglaciation.



759

760

Figure 7: Difference between EH and LGM $\delta^{15}\text{N}$ at 4 different polar sites (raw data are given in Supplementary Table S4).

761

The measured $\delta^{15}\text{N}$ difference is shown by a black bar (data). The modelled $\delta^{15}\text{N}$ difference is shown with colours: old

762

version in red (orange with the impurity influence), new version in blue with different parameterizations. “New”

763

corresponds to the parameterization of Table 1. Parameterizations for sensitivity tests A, B, C and D are given in Table

764

3. When “+ dust” is mentioned, it corresponds to the addition of the impurity influence as parameterized by Freitag et

765

al., (2013) (Equations 8 and 9). Test Pimienta-Barnola (P-B) corresponds to a test with implementation of the impurity

766

effect in the “New” parameterization following the Freitag parameterization adapted to the Pimienta-Barnola model

767

instead of the Herron and Langway model used for the other sensitivity tests. We display the modelled error bars only

768

on the old model outputs (red) but the same uncertainty can be applied to all model outputs (New, Tests A, B, C, D and

769

P-B) at each site.

770

771

3.2.3 Results with updated temperature parameterization

772

773

By construction, the new LGGE firn model with the temperature dependency of the firn densification

774

module depicted on Section 2.2.1 is expected to improve the agreement between model and data

775

for cold sites of East Antarctica over the last deglaciation by increasing densification rates at low

776

temperature. This new parameterization modifies the densification rate through the creep

777

parameter given in Equation (7). Figure 8 shows the evolution of the creep parameter with

778

temperature for different choices of the three activation energies Q_1 , Q_2 and Q_3 . Compared to the

779

old model, the densification rate is higher at low temperature, below -55°C (i.e. for LGM at Dome C

780

and Vostok, Table 1). At higher temperature (between -55°C and -28°C corresponding to present-

781

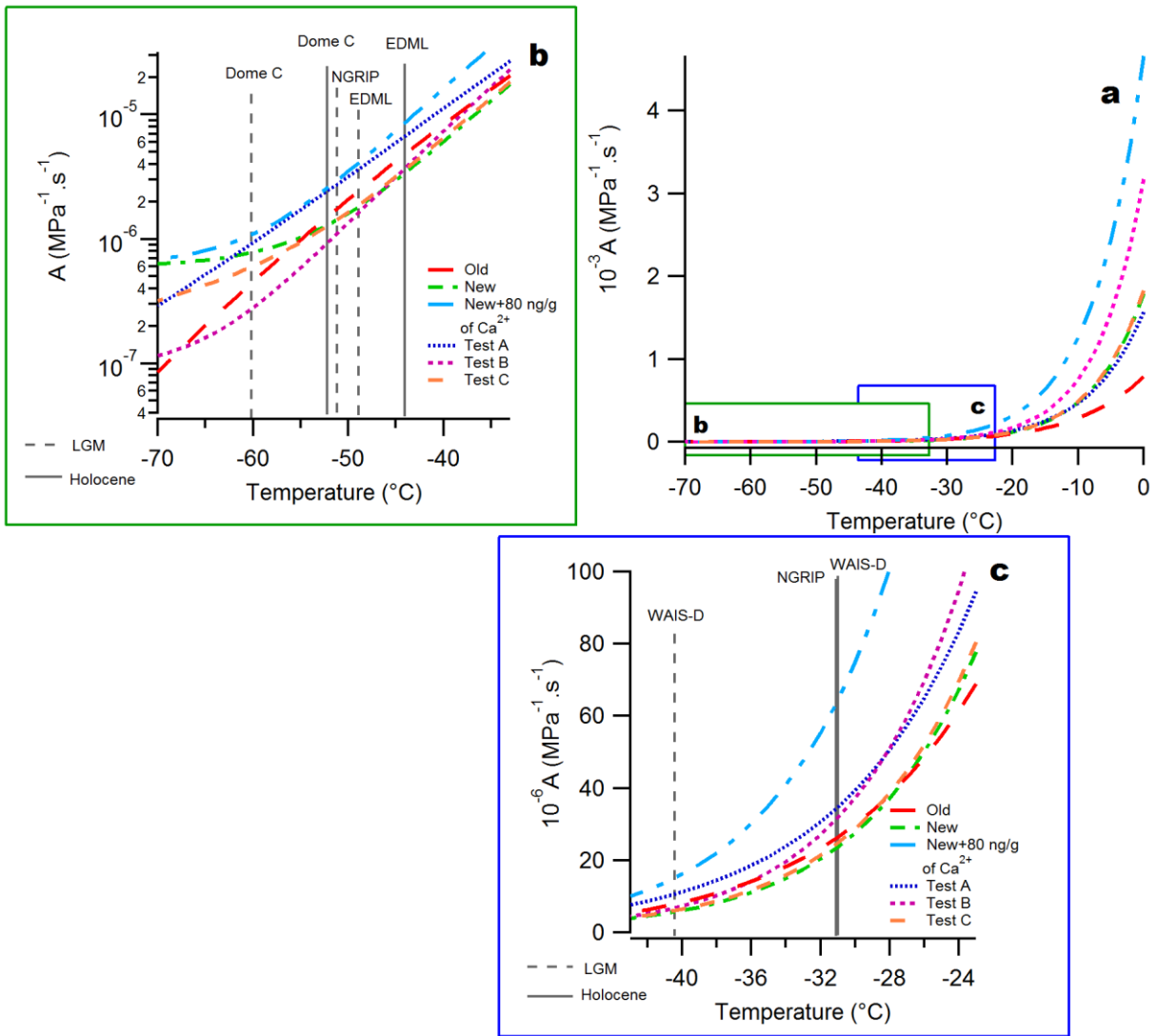
day temperature in most polar sites), the creep parameter is slightly lower than in the old model.

782

The difference between the 2 curves is however not large so that densification rate is not strongly

783 modified over this range. This is in agreement with comparable firn density profiles obtained for the
784 different polar sites using the old or the improved LGGE model (Section 3.1, Figure 4).

785 In the improved model, the simulated profiles of $\delta^{15}\text{N}$ are comparable to $\delta^{15}\text{N}$ simulated with the
786 old model at the sites that were already showing a good agreement between the old model outputs
787 and data, for example NGRIP, GISP-2, Talos Dome and WAIS-Divide (Figure 6 and Supplementary
788 Figure S8). This is expected since the corresponding densification rate is only slightly reduced in the
789 temperature range of $-55^\circ\text{C}/-28^\circ\text{C}$ which corresponds to the temperature range encompassed over
790 the last deglaciation at these sites. This results in a deeper LID and hence higher $\delta^{15}\text{N}$ level, which is
791 in general compatible with the data (except at Talos Dome). Some differences are also observed for
792 the timing of the $\delta^{15}\text{N}$ peaks for Bølling-Allerød and end of Younger Dryas at NGRIP when using the
793 different model versions reflecting variations in the simulated Δage (cf Supplementary Table S5);
794 the general agreement with the measured profile is preserved with even a slight improvement of
795 the modelled Δage with $\delta^{15}\text{N}$ constraints with the modified model. At the coldest sites (Dome C,
796 Vostok), the agreement between data and modelled profiles is largely improved with a modelled
797 LGM $\delta^{15}\text{N}$ smaller than the modelled EH $\delta^{15}\text{N}$, but a perfect match cannot be found. At the
798 intermediate EDML site, it is not possible to reproduce the sign of the slope during the deglaciation.
799
800



801
 802 *Figure 8: Dependence of the creep parameter (Equation 7) as a function of temperature for 6 different*
 803 *parameterizations. “Old” corresponds to the Goujon et al. (2003) version of the model; “New” corresponds to*
 804 *the improved LGGE model with parameterization described in Table 1; “New + 80 ng/g of Ca²⁺” corresponds*
 805 *to the parameterization of Table 1 with the addition of the impurity effect following Equation (8) and a [Ca²⁺]*
 806 *value of 80 ng/g; Tests A, B and C are sensitivity tests run with the values presented on Table 3. Figure 8a*
 807 *shows the creep parameter evolution for the whole temperature range, Figure 8b is a focus at very low*
 808 *temperature and Figure 8c is a focus at intermediate temperature. The grey vertical lines indicates the*
 809 *temperature for Early Holocene (EH, solid line) and LGM (dotted line) at the 4 study sites presented in Figures*
 810 *6 and 7.*

811

Test	Activation energy (J/mol)	Coefficient
Test A	$Q_1 = 90000$	$a_1 = 5.5 \cdot 10^5$
	$Q_2 = 60000$	$a_2 = 1.0$
	$Q_3 = 30000$	$a_3 = 4.5 \cdot 10^{-8}$
Test B	$Q_1 = 110000$	$a_1 = 5.5 \cdot 10^9$
	$Q_2 = 75000$	$a_2 = 1950.0$

	$Q_3 = 1500$	$a_3 = 9.0 \cdot 10^{-16}$
Test C	$Q_1 = 110000$	$a_1 = 1.05 \cdot 10^9$
	$Q_2 = 75000$	$a_2 = 1400$
	$Q_3 = 15000$	$a_3 = 8.7 \cdot 10^{-12}$
Test D	$Q_1 = 110000$	$a_1 = 1.05 \cdot 10^9$
	$Q_2 = 75000$	$a_2 = 980$
	$Q_3 = 1230$	$a_3 = 3.6 \cdot 10^{-15}$

812

813

814

815

816

817

Table 3: Values used for the different sensitivity tests for three activation energies. These values have been chosen to illustrate the effects of varying activation energy for the different temperature ranges on the densification rate for the different ice core deep drilling sites (cf figure 8) and support the tuning presented on Table 1.

818

819

820

821

822

823

In order to more quantitatively assess the robustness of the proposed parameterization in Table 1, we confront in Figure 7 the measured and modelled $\delta^{15}\text{N}$ differences between the LGM and EH at the 4 Greenland and Antarctic sites selected in Figure 7 above. For this comparison, we use not only the parameterization of Table 1 but also sensitivity tests performed with different parameterizations of the temperature dependency of activation energy and impurity effects (details on Table 3).

824

825

826

827

When using the parameterization of Table 1 (“new model”), Figure 7 shows strong improvement of the simulation of the $\delta^{15}\text{N}$ difference between EH and LGM at Vostok and Dome C. Indeed, the modelled EH-LGM difference now has the correct sign at very cold sites of East Antarctica (Figure 7) when compared with $\delta^{15}\text{N}$ measurements.

828

829

830

831

832

833

834

835

836

837

838

839

840

We present some sensitivity tests to illustrate the choice of our final parameterization (i.e. the new model) through influences on the creep parameters and LGM vs EH $\delta^{15}\text{N}$ changes. As displayed in Figure 8, test A has a higher creep parameter than the old model throughout the whole temperature range. Compared to the output of the old model, the LGM vs EH $\delta^{15}\text{N}$ change simulated with test A is slightly higher but the sign of the $\delta^{15}\text{N}$ change over the last deglaciation is still wrong at Dome C and EDML. This test shows that it is not the mean value of the creep parameter that needs to be changed, but the dependency to temperature. Test B has a higher creep parameter above -35°C , but a lower creep parameter than the old model below -35°C , which starts flattening and hence reaching values higher than the old model creep parameter below -65°C . The LGM vs EH $\delta^{15}\text{N}$ change simulated with test B is still comparable with data at WAIS-Divide. However, the model – data comparison deteriorates at NGRIP and EDML compared to the model-data comparison with the old version of the model. Moreover, it does not solve the model – data mismatch at Dome C. This shows that the change in the creep parameter at intermediate temperature is too steep. Strong differences

841 occur at high temperature (above -30°C) but it does not affect the modelled $\delta^{15}\text{N}$ change between
842 LGM and EH for our 4 sites. On the contrary, the slightly lower creep parameter at low temperature
843 leads to a worse agreement between model and data for the Dome C deglaciation than when using
844 the “new model”. Test C has been designed so that the activation energy at low temperature
845 corresponds to estimates of activation energy for ice surface diffusion (Jung et al., 2004; Nie et al.,
846 2009), a mechanism that is expected to be important at low temperature (Ashby, 1974). Using such
847 a parameterization leads to a fair agreement between the modelled and the measured $\delta^{15}\text{N}$ change
848 over the last deglaciation for the different sites. At Dome C, the correct sign for the $\delta^{15}\text{N}$ evolution
849 between LGM and the Holocene is predicted by the model. However, the modelled $\delta^{15}\text{N}$ increase is
850 still too small compared to the data and the $\delta^{15}\text{N}$ calculated by the “new model”. This is probably
851 due to a too high creep parameter at low temperature.

852 Summarizing, the best agreement between data and model for Dome C is obtained for the
853 parameters given on Table 1: the creep parameter of “new model” flattens below -50°C and is thus
854 not very different for the LGM or the EH at Dome C. As a result, the modelled LID and hence $\delta^{15}\text{N}$
855 are less sensitive to temperature, and the sign of the EH-LGM difference can be inverted, and
856 brought closer to the observations. It should be noted that despite many sensitivity tests we could
857 not find a parameterization able to reproduce the EH-LGM $\delta^{15}\text{N}$ changes for all 4 sites. In the “new
858 model” without impurity effect, it is not possible to reproduce the measured EDML $\delta^{15}\text{N}$ change
859 over the last deglaciation even when taking into account the uncertainty in the input parameters
860 (temperature and accumulation rate, Supplementary Figure S9).

861

862 3.2.4 Impurity softening

863

864 The dust content in LGM ice is much larger than in Holocene ice (Figure 6), and impurity inclusions
865 in ice have an impact on the grain structure, allowing it to deform more easily (Alley, 1987; Fujita et
866 al., 2014). We incorporated dust softening using the parameterization of Freitag et al (2013) as
867 detailed in Section 2.2.2. We compared two expressions for the impurity softening (tuned to be
868 applied to the Herron and Langway model, or Pimienta and Barnola model), but found that the
869 differences between the two parameterisations were minor (Figure 7). We use the Herron and
870 Langway parameters in the following.

871

872 Figure 8 shows the effect of impurities on the creep parameter: densification is enhanced over the
873 whole temperature range. At all sites, incorporating impurity softening reduces the firn thickness

874 during periods characterized by high impurity concentration in the ice (LGM). It thus leads to an
875 increase of the EH-LGM LID difference (Figure 7).

876

877 This effect clearly helps to bring in agreement modelled and measured $\delta^{15}\text{N}$ at Dome C, Vostok and
878 EDML (Figures 6, 7 and Supplementary Figure S8). The improvement through dust softening is
879 particularly important at EDML where the change of activation energy had only a modest effect. For
880 the 3 sites mentioned above, the model incorporating the parameterization of activation energy
881 depicted in Table 1 and the impurity effects is able to reproduce the $\delta^{15}\text{N}$ increase over the last
882 deglaciation. Note that short-lived peaks in impurities, likely triggered by volcanic events, have no
883 visible effect on bulk firn thickness (Figure 6). Contrary to the improved situation in cold Antarctic
884 sites, we observe that, at the warmer sites like NGRIP and WAIS-Divide, incorporating impurity
885 softening deteriorates the model data fit, which was already good in the older version of the model,
886 and also good with other firn densification models (Kindler et al, 2014; Buizert et al, 2015). It
887 produces almost no change in firn thickness between the LGM and the EH at NGRIP, which
888 contradicts $\delta^{15}\text{N}$ observations. The same mismatch is observed at WAIS-Divide using a different
889 model, as already noted by Buizert et al. (2015). We tested the sensitivity to the dust
890 parameterization by implementing the Freitag parameterization adapted to the Pimienta-Barnola
891 model instead of the parameters for the Herron and Langway model used with our improved model
892 (cf Section 2.2.2). The two different parameterizations of the impurity effect lead to very
893 comparable LGM to EH $\delta^{15}\text{N}$ changes over the last deglaciation on the 4 sites discussed here.

894 The model – data mismatch observed when incorporating the dust effect may be partially due to
895 the fact that we did not readjust a_i and Q_i after implementation of the impurity effect. To explore
896 this possibility, sensitivity test D has been designed with a re-parameterization of the a_i and Q_i values
897 after implementation of the impurity effect. To do so, we calculated the optimal creep parameter A
898 for each mean EH and LGM condition at each site, and adjusted sequentially a_3 , a_2 , a_1 , Q_3 , Q_2 , and
899 Q_1 to minimize the model-data mismatch. Only a_3 , a_2 and Q_3 needed adjustments, and their values
900 can be found in Table 3. We did not perform the adjustment on modern density profiles, because
901 these are only weakly sensitive to the dust parameterization, Ca^{2+} concentrations being low.

902 Impurity concentration is very high at NGRIP during the glacial period. As a consequence, even if our
903 new parameterization of a_i and Q_i (new model) properly reproduces the Greenland $\delta^{15}\text{N}$ level at the
904 LGM, this glacial modelled Greenland $\delta^{15}\text{N}$ level is too low when including the impurity effect. The
905 re-parameterization of a_i and Q_i , proposed as sensitivity test D, enables an improvement of the

906 agreement between model and data for glacial $\delta^{15}\text{N}$ at WAIS-Divide, maintain the results at Dome-
907 C and EDML, but can still not produce reasonable results at NGRIP (Figure 7).

908

909 The mismatch observed for the $\delta^{15}\text{N}$ simulations at WAIS-Divide and NGRIP when incorporating the
910 impurity effect suggests that the parameterization presented in Equations (8) and (9) is not
911 appropriate to be used on bulk $[\text{Ca}^{2+}]$ concentration and/or for LGM simulation. Actually, the
912 proposed parameterization by Freitag et al. (2013) was tuned to density variability in present-day
913 firn, and may not be valid for LGM when $[\text{Ca}^{2+}]$ concentrations were 10-100 times larger than
914 present-day. It is also possible that the dust effect saturates at high concentration, and is no longer
915 sensitive above a certain threshold. To further improve the model – data agreement with the dust
916 parameterization, a possibility is to add simple thresholds on a minimum and maximum effect of
917 calcium as proposed in supplementary material (Supplementary Text S2 and Figure S10).
918 Implementing threshold values on calcium reduces the largest inconsistencies between model
919 results and $\delta^{15}\text{N}$ data, in particular at NGRIP (through the threshold at high calcium concentration)
920 and at WAIS (through the threshold at low calcium concentration).

921

922 It is also possible that the impurity influence, like temperature, acts differently depending on the
923 dominant mechanism for firn deformation, and that the impurity effect is more important at colder
924 temperature. The mechanisms by which impurities influence firn deformation are still poorly
925 understood. Dust particles do not always influence densification in the same way: dissolved particles
926 soften firn and ice while the softening or hardening effect of non-dissolved impurities is less clear
927 (Fujita et al., 2016; Alley et al., 1987). More work is thus needed before the correct “impurity effect”
928 component and the mechanisms by which it acts on densification are identified (e.g. Fujita et al.,
929 2014, 2016). Here, we have shown that a simple parameterization as a function of $[\text{Ca}^{2+}]$
930 concentration does not provide uniformly good results, and seems only suitable for sites on the
931 Antarctic Plateau.

932

933 To sum up, the new parameterization of the creep parameter has been designed to preserve good
934 agreement between the old model outputs and data at sites that were already well simulated
935 (WAIS-Divide, NGRIP, Talos Dome). In addition, this parameterization improves the simulation of
936 the deglaciation at cold Antarctic Sites (Dome C, Vostok). However, the EH-LGM $\delta^{15}\text{N}$ change at
937 Dome C and EDML cannot be reproduced using only the temperature dependency of activation
938 energy. The inclusion of impurity effect following the Freitag parameterization improves the

939 situation for cold sites but leads to inconsistent $\delta^{15}\text{N}$ evolutions over the deglaciation at WAIS-Divide
940 and NGRIP unless threshold effects are implemented.

941

942 4. Conclusion and perspectives

943

944 In this study, we have presented a revision of the LGGE firn densification model. We have
945 summarized the parameterization choices of this firn model that would explain a large part of the
946 disagreement between modelled and measured $\delta^{15}\text{N}$ evolution over the last deglaciation for
947 extremely cold sites of East Antarctica. Based on analogy with ceramic sintering at hot temperature
948 and recent observations of the impurity effect on firn density, we have improved the LGGE
949 densification model by incorporating new parameterizations for the evolution of the creep
950 parameter with temperature and impurity contents within the firn densification module. We follow
951 previous studies evidencing different dominant firn sintering mechanisms for different temperature
952 ranges that support a temperature dependency of the creep activation energy. We showed that
953 these new parameterizations improve the agreement between model and data at low temperature
954 (below -30°C), and retain the good agreement at warmer temperature. In particular, the improved
955 LGGE firn density model is now able to reproduce the $\delta^{15}\text{N}$ increase over deglaciations at cold sites
956 such as Dome C and Vostok.

957

958 The new parameterization implies a more rapid firn densification at lower temperature and high
959 impurity load than in classical firnification models. This result obtained with our associated
960 appropriate parameterization is in agreement with the study of Parrenin et al. (2012) showing that
961 the classical firn densification model overestimates LID during the last glacial period at EDC. With
962 our revised model, the simulated Δage is also significantly decreased for the glacial periods at low
963 accumulation and temperature sites of the East Antarctic plateau (Dome C, Vostok and Dome Fuji).
964 This has important consequences for building air vs ice timescales in Antarctica and hence for the
965 studies of the relationships between temporal evolutions of atmospheric composition vs. Antarctic
966 temperature. At EDC 21 ka (ice age), the modelled Δage decreases from 4840 years (old model) to
967 4270 years (new model) or 4200 years (new model including impurity effect). At Vostok 21 ka (ice
968 age), the modelled Δage decreases from 5630 years (old model) to 5030 years (new model) or 4900
969 years (new model including impurity effect). The latest results are in good agreement with the
970 recent determination of Δage within the AICC2012 timescale: 3920 years for EDC 21 ka (ice age) and
971 5100 years for Vostok 21 ka (ice age). This is not unexpected since the EDC LID in the construction

972 of the AICC2012 timescale is deduced from the EDC $\delta^{15}\text{N}$ scenario, a hypothesis supported by the
973 available gas and ice stratigraphic markers over the last deglaciation (Parrenin et al., 2012).

974

975 Our finding is, however, associated with several limitations so that this new model does not propose
976 a definite re-evaluation of the formulation of the activation energy but proposes some ways to be
977 further tested and explored to improve firn densification models especially for applications in
978 paleoclimate reconstructions. Our approach remains empirical and we could not identify separately
979 the different mechanisms involved. The problem of a $\delta^{15}\text{N}$ data-model mismatch in low temperature
980 and accumulation rate sites of East Antarctica is thus not definitively solved. Still, we showed that
981 revising the temperature and impurity dependence of firn densification rate can potentially strongly
982 reduce the $\delta^{15}\text{N}$ data-model mismatch and proposed preliminary parameterizations easy to
983 implement in any firn densification model.

984 Finally, the new parameterization proposed here calls for further studies. First, laboratory or field
985 studies of firn densification at very cold controlled conditions are needed to check the
986 predominance of one mechanism over another at low temperature such as the predominance of
987 the boundary diffusion over grain boundary mechanism around -60°C ; this is a real challenge
988 because of the slow speed of deformation. Second, we have suggested that the current
989 parameterization of impurity on firn softening should be revised, especially for very high impurity
990 load (Greenland) using for example thresholds on impurity concentrations. Third, the separate
991 effects of impurities and temperature on firn densification and hence $\delta^{15}\text{N}$ evolution should be
992 tested on periods other than the last deglaciation. Sequences of events associated with non-
993 synchronous changes in surface temperature, accumulation rate and impurity content would be
994 particularly valuable for this objective. Finally, additional constraints on the firn modelling can also
995 be obtained through the use of cross-dating on new ice core with high resolution signals as already
996 used by Parrenin et al. (2012).

997

998 *Acknowledgements:* We thank Anders Svensson, Rob Arthern, Hans Christian Steen-Larsen and Xiao
999 Cunde for data sharing and Sarah Guilbaud for her work during her final internship study. Thanks to
1000 Pierre Badel, Maurine Montagnat and Christophe Martin for insightful discussions about
1001 densification mechanisms. Thanks to Myriam Guillevic for her work on the densification model and
1002 helpful discussions. This work is supported by INSU/CNRS LEFE project NEVE-CLIMAT and the ERC
1003 COMBINISO 306045.

1004

1005

1006 References

1007

1008 Alley, R. B.: Firn densification by grain-boundary sliding: a first model, *J. Phys. Colloq.*, 48(C1), C1-
1009 249-C1-256, doi:10.1051/jphyscol:1987135, 1987.

1010 Altnau, S., Schlosser, E., Isaksson, E. and Divine, D., Climatic signals from 76 shallow firn cores in
1011 Dronning Maud Land, East Antarctica, *The Cryosphere Discussions*, Volume 8, Issue 6, pp. 5961-
1012 6005, 2014.

1013 Anderson, D. L. and Benson, C. S.: The densification and diagenesis of snow, in *Ice and Snow: Properties, Processes and Applications*, pp. 391–411, MIT Press., 1963.

1015 Arnaud, L.: Modélisation de la transformation de la neige en glace à la surface des calottes polaires; Etude du transport des gaz dans ces milieux poreux, PhD Thesis, Université Joseph Fournier -
1016 Grenoble 1, 294 pp, 1997.

1018 Arnaud, L., Barnola, J. M. and Duval, P.: Physical modeling of the densification of snow/firn and ice
1019 in, *Phys. Ice Core Rec.*, 26, 39–44, 2000.

1020 Arthern, R. J., Vaughan, D. G., Rankin, A. M., Mulvaney, R. and Thomas, E. R.: In situ measurements
1021 of Antarctic snow compaction compared with predictions of models, *J. Geophys. Res.*, 115(F3),
1022 doi:10.1029/2009JF001306, 2010.

1023 Arzt, E.: The influence of an increasing particle coordination on the densification of spherical
1024 powders, *Acta Metall.*, 30(10), 1883–1890, 1982.

1025 Arzt, E., Ashby, M. F. and Easterling, K. E.: Practical applications of hot-isostatic pressing diagrams:
1026 four case studies, *Metall. Trans. A*, 14(1), 211–221, 1983.

1027 Ashby M. F., A first report on sintering diagrams, *Acta Metallurgica*, vol. 22, 1974.

1028 Barnes, P., Tabor, D. and Walker, J. C. F.: The friction and creep of polycrystalline ice, in *Proceedings of the Royal Society of London A: Mathematical, Physical and Engineering Sciences*, vol. 324, pp. 127–155, The Royal Society, 1971.

1031 Barnola, J.-M., Pimienta, P., Raynaud, D. and Korotkevich, Y. S.: CO₂-climate relationship as deduced
1032 from the Vostok ice core: a re-examination based on new measurements and on a re-evaluation of
1033 the air dating, *Tellus B*, 43(2), 83–90, 1991.

1034 Bazin, L., Landais, A., Lemieux-Dudon, B., Toyé Mahamadou Kele, H., Veres, D., Parrenin, F.,
1035 Martinerie, P., Ritz, C., Capron, E., Lipenkov, V., Loutre, M-F., Vinther, B., Svensson, A., Rasmussen,
1036 S. O., Severi, M., Blunier, T., Leuenberger, M., Fischer, H., Masson-Delmotte, V., Chapellaz, J., and
1037 Wolff E.: An optimized multi-proxy, multi-site Antarctic ice and gas orbital chronology (AICC2012):
1038 120-800 ka, *Clim. Past*, 9(4), 1715–1731, 2013.

1039 Bender M. L., Sowers T., Barnola J.-M. and Chappellaz J., Changes in the O₂/N₂ ratio of the
1040 atmosphere during recent decades reflected in the composition of air in the firn at Vostok Station,
1041 Antarctica, *Geophysical Resaerch Letters*, vol. 21, N. 3, 189-192, 1994.

1042

- 1043 Bender, M. L., Floch, G., Chappellaz, J., Suwa, M., Barnola, J.-M., Blunier, T., Dreyfus, G., Jouzel, J.
1044 and Parrenin, F.: Gas age–ice age differences and the chronology of the Vostok ice core, 0–100 ka,
1045 *J. Geophys. Res.*, 111(D21), doi:10.1029/2005JD006488, 2006.
- 1046 Benson, C. S.: Stratigraphic studies in the snow and firn of the Greenland ice sheet, PhD Thesis,
1047 California Institute of Technology, pp 228, 1960.
- 1048 Blackford, J. R.: Sintering and microstructure of ice: a review, *J. Phys. Appl. Phys.*, 40(21), R355–
1049 R385, doi:10.1088/0022-3727/40/21/R02, 2007.
- 1050 Buizert, C., Sowers, T. and Blunier, T.: Assessment of diffusive isotopic fractionation in polar firn, and
1051 application to ice core trace gas records, *Earth Planet. Sci. Lett.*, 361, 110–119,
1052 doi:10.1016/j.epsl.2012.11.039, 2013.
- 1053 Buizert, C., Gkinis, V., Severinghaus, J. P., He, F., Lecavalier, B. S., Kindler, P., Leuenberger, M.,
1054 Carlson, A. E., Vinther, B., Masson-Delmotte, V., White, J. W. C., Liu, Z., Otto-Bliesner, B. and Brook,
1055 E. J.: Greenland temperature response to climate forcing during the last deglaciation, *Science* ,
1056 345(6201), 1177–1180, doi:10.1126/science.1254961, 2014.
- 1057 Buizert, C., Cuffey, K. M., Severinghaus, J. P., Baggenstos, D., Fudge, T. J., Steig, E. J., Markle, B. R.,
1058 Winstrup, M., Rhodes, R. H., Brook, E. J., Sowers, T. A., Clow, G. D., Cheng, H., Edwards, R. L., Sigl,
1059 M., McConnell, J. R. and Taylor, K. C.: The WAIS Divide deep ice core WD2014 chronology-Part 1:
1060 Methane synchronization (68–31 ka BP) and the gas age–ice age difference, *Clim. Past*, 11(2), 153–
1061 173, doi:10.5194/cp-11-153-2015, 2015.
- 1062 Capron, E., Landais, A., Buiron, D., Cauquoin, A., Chappellaz, J., Debret, M., Jouzel, J., Leuenberger,
1063 M., Martinerie, P., Masson-Delmotte, V., Mulvaney, R., Parrenin, F. and Prié, F.: Glacial–interglacial
1064 dynamics of Antarctic firn columns: comparison between simulations and ice core air- $\delta^{15}\text{N}$
1065 measurements, *Clim. Past*, 9(3), 983–999, doi:10.5194/cp-9-983-2013, 2013.
- 1066 Cauquoin, A., Landais, A., Raisbeck, G. M., Jouzel, J., Bazin, L., Kageyama, M., Peterschmitt, J.-Y.,
1067 Werner, M., Bard, E. and ASTER Team, Comparing past accumulation rate reconstructions in East
1068 Antarctic ice cores using ^{10}Be , water isotopes and CMIP5-PMIP3 models, *Climate of the Past*, 11,
1069 355-367, 2015.
- 1070 Colbeck, S. C.: Theory of metamorphism of dry snow, *J. Geophys. Res. Oceans*, 88(C9), 5475–5482,
1071 1983.
- 1072 Craig, H., Horibe, Y. and Sowers, T.: Gravitational separation of gases and isotopes in polar ice caps,
1073 *Science*, 242(4886), 1675–1678, 1988.
- 1074 Cuffey, K. M. and Clow, G. D.: Temperature, accumulation, and ice sheet elevation in central
1075 Greenland through the last deglacial transition, *J. Geophys. Res. Oceans*, 102(C12), 26383–26396,
1076 1997.
- 1077 Cuffey, K. M., Clow, G. D., Steig, E. J., Buizert, C., Fudge, T. J., Koutnik, M., Waddington E. D., Alley,
1078 R. B. and Severinghaus, J. P., Deglacial temperature history of West Antarctica, *PNAS*, vol 11, no. 50,
1079 14249-14254, 2016.
- 1080 Dahl-Jensen, D.: Past Temperatures Directly from the Greenland Ice Sheet, *Science*, 282(5387), 268–
1081 271, doi:10.1126/science.282.5387.268, 1998.

- 1082 Dee, D. P., Uppala, S. M., Simmons, A. J., Berrisford, P., Poli, P., Kobayashi, S., Andrae, U., Balmaseda,
1083 M. A., Balsamo, G., Bauer, P., Bechtold, P., Beljaars, A. C. M., van de Berg, L., Bidlot, J., Bormann, N.,
1084 Delsol, C., Dragani, R., Fuentes, M., Geer, A. J., Haimberger, L., Healy, S. B., Hersbach, H., Hólm, E.
1085 V., Isaksen, I., Kållberg, P., Köhler, M., Matricardi, M., McNally, A. P., Monge-Sanz, B. M., Morcrette,
1086 J.-J., Park, B.-K., Peubey, C., de Rosnay, P., Tavolato, C., Thépaut, J.-N. and Vitart, F.: The ERA-Interim
1087 reanalysis: configuration and performance of the data assimilation system, *Q. J. R. Meteorol. Soc.*,
1088 137(656), 553–597, doi:10.1002/qj.828, 2011.
- 1089 Dreyfus, G. B., Jouzel, J., Bender, M. L., Landais, A., Masson-Delmotte, V. and Leuenberger, M.: Firn
1090 processes and $\delta^{15}\text{N}$: potential for a gas-phase climate proxy, *Quat. Sci. Rev.*, 29(1–2), 28–42,
1091 doi:10.1016/j.quascirev.2009.10.012, 2010.
- 1092 Ebinuma, T. and Maeno, N.: Particle rearrangement and dislocation creep in a snow-densification
1093 process, *J. Phys. Colloq.*, 48(C1), C1-263-C1-269, doi:10.1051/jphyscol:1987137, 1987.
- 1094 EPICA community members: Eight glacial cycles from an Antarctic ice core, *Nature*, 429(6992), 623–
1095 628, 2004.
- 1096 Freitag, J., Kipfstuhl, S., Laepple, T. and Wilhelms, F.: Impurity-controlled densification: a new model
1097 for stratified polar firn, *J. Glaciol.*, 59(218), 1163–1169, doi:10.3189/2013JoG13J042, 2013.
- 1098 Frieler, K., Clark, P. U., He, F., Buizert, C., Reese, R., Ligtenberg, S. R. M., van den Broeke, M. R.,
1099 Winkelmann, R. and Levermann, A.: Consistent evidence of increasing Antarctic accumulation with
1100 warming, *Nat. Clim. Change*, 5(4), 348–352, doi:10.1038/nclimate2574, 2015.
- 1101 Fujita, S., Hirabayashi, M., Goto-Azuma, K., Dallmayr, R., Satow, K., Zheng, J. and Dahl-Jensen, D.:
1102 Densification of layered firn of the ice sheet at NEEM, Greenland, *J. Glaciol.*, 60(223), 905–921,
1103 doi:10.3189/2014JoG14J006, 2014.
- 1104 Fujita, S., Goto-Azuma, K., Hirabayashi, M., Hori, A., Iizuka, Y., Motizuki, Y., Motoyama, H. and
1105 Takahashi, K.: Densification of layered firn in the ice sheet at Dome Fuji, Antarctica, *J. Glaciol.*,
1106 62(231), 103–123, doi:10.1017/jog.2016.16, 2016.
- 1107 Goujon, C., Barnola, J.-M. and Ritz, C.: Modeling the densification of polar firn including heat
1108 diffusion: Application to close-off characteristics and gas isotopic fractionation for Antarctica and
1109 Greenland sites, *J. Geophys. Res. Atmospheres*, 108(D24), 2003.
- 1110 Gow, A. J.: Deep core studies of the accumulation and densification of snow at Byrd station and
1111 Little America V, Antarctica, CRREL Research Report 197, 1968.
- 1112 Grachev A. M. and Severinghaus J. P., Determining the thermal diffusion factor for Ar-40/Ar-36 in
1113 air to aid paleoreconstruction of abrupt climate change, *The Journal of Physical Chemistry*, 107(23),
1114 pp 4636-4642, 2003.
- 1115 Guillevic, M., Bazin, L., Landais, A., Kindler, P., Orsi, A., Masson-Delmotte, V., Blunier, T., Buchardt,
1116 S. L., Capron, E., Leuenberger, M., Martinerie, P., Prié, F. and Vinther, B. M.: Spatial gradients of
1117 temperature, accumulation and $\delta^{18}\text{O}$ -ice in Greenland over a series of Dansgaard-Oeschger events,
1118 *Clim. Past*, 9(3), 1029–1051, doi:10.5194/cp-9-1029-2013, 2013.
- 1119 Hagenmuller, P., Chambon, G. and Naaim, M.: Microstructure-based modeling of snow mechanics:
1120 a discrete element approach, *The Cryosphere*, 9(5), 1969–1982, doi:10.5194/tc-9-1969-2015, 2015.

- 1121 Helsen, M. M., van den Broeke, M. R., van de Wal, R. S. W., van de Berg, W. J., van Meijgaard, E.,
 1122 Davis, C. H., Li, Y. and Goodwin, I.: Elevation Changes in Antarctica Mainly Determined by
 1123 Accumulation Variability, *Science*, 320(5883), 1626–1629, doi:10.1126/science.1153894, 2008.
- 1124 Herron, M. M. and Langway, C. C.: Firn densification: an empirical model, *J. Glaciol.*, 25(93), 373–
 1125 385, 1980.
- 1126 Hörhold, M. W., Laepple, T., Freitag, J., Bigler, M., Fischer, H. and Kipfstuhl, S.: On the impact of
 1127 impurities on the densification of polar firn, *Earth Planet. Sci. Lett.*, 325, 93–99, 2012.
- 1128 Jacka, T. H. and Li, J.: The steady-state crystal size of deforming ice, *Ann. Glaciol.*, 20(1), 13–18, 1994.
- 1129 Jouzel, J.: Magnitude of isotope/temperature scaling for interpretation of central Antarctic ice cores,
 1130 *J. Geophys. Res.*, 108(D12), doi:10.1029/2002JD002677, 2003.
- 1131 Jouzel, J., Masson-Delmotte, V., Cattani, O., Dreyfus, G., Falourd, S., Hoffmann, G., Minster, B.,
 1132 Nouet, J., Barnola, J. M., Chappellaz, J., Fischer, H., Gallet, J. C., Johnsen, S., Leuenberger, M.,
 1133 Loulergue, L., Luethi, D., Oerter, H., Parrenin, F., Raisbeck, G., Raynaud, D., Schilt, A., Schwander, J.,
 1134 Selmo, E., Souchez, R., Spahni, R., Stauffer, B., Steffensen, J. P., Stenni, B., Stocker, T. F., Tison, J. L.,
 1135 Werner, M. and Wolff, E. W.: Orbital and Millennial Antarctic Climate Variability over the Past
 1136 800,000 Years, *Science*, 317(5839), 793–796, doi:10.1126/science.1141038, 2007.
- 1137 Jung K.-H., Park, S.-C., Kim, J.-H. and Kang, H., Vertical diffusion of water molecules near the surface
 1138 of ice, *Journal of Chemical Physics*, vol. 121, No. 6, DOI: 10.1063/1.1770518, 2004.
- 1139 Kapsner, W. R., Alley, R. B., Shuman, C. A., Anandakrishnan, S. and Grootes, P. M.: Dominant
 1140 influence of atmospheric circulation on snow accumulation in Greenland over the past 18,000 years,
 1141 *Nature*, 373(6509), 52–54, 1995.
- 1142 Kawamura K., Severinghaus J. P., Ishidoya S., Sugawara S., Hashida G., Motoyama H., Fujii Y., Aoki S.
 1143 and Nakazawa T., Convective mixing of air in firn at four polar sites, *Earth and Planetary Science*
 1144 *Letters*, 244, 672-682, 2006.
- 1145 Kindler, P., Guillevic, M., Baumgartner, M., Schwander, J., Landais, A., Leuenberger, M., Spahni, R.,
 1146 Capron, E. and Chappellaz, J.: Temperature reconstruction from 10 to 120 kyr b2k from the NGRIP
 1147 ice core, *Clim. Past*, 10(2), 887–902, doi:10.5194/cp-10-887-2014, 2014.
- 1148 Köhler, P., Knorr, G., Buiron, D., Lourantou, A., & Chappellaz, J., Abrupt rise in atmospheric CO₂ at
 1149 the onset of the Bølling/Allerød: in-situ ice core data versus true atmospheric signal, *Climate of the*
 1150 *Past*, 7(2), 473-486, 2011.
- 1151 Kojima, K.: Densification of seasonal snow cover, *Phys. Snow Ice Proc. HUSCAP*, 1(2), 929–952, 1967.
- 1152 Landais, A., Barnola, J. M., Kawamura, K., Caillon, N., Delmotte, M., Van Ommen, T., Dreyfus, G.,
 1153 Jouzel, J., Masson-Delmotte, V., Minster, B., Freitag, J., Leuenberger, M., Schwander, J., Huber, C.,
 1154 Etheridge, D. and Morgan, V.: Firn-air $\delta^{15}\text{N}$ in modern polar sites and glacial–interglacial ice: a
 1155 model-data mismatch during glacial periods in Antarctica?, *Quat. Sci. Rev.*, 25(1–2), 49–62,
 1156 doi:10.1016/j.quascirev.2005.06.007, 2006.
- 1157 Landais, A., Dreyfus, G., Capron, E., Jouzel, J., Masson-Delmotte, V., Roche, D. M., Prié, F., Caillon,
 1158 N., Chappellaz, J., Leuenberger, M., Lourantou, A., Parrenin, F., Raynaud, D. and Teste, G.: Two-
 1159 phase change in CO₂, Antarctic temperature and global climate during Termination II, *Nat. Geosci.*,
 1160 6(12), 1062–1065, doi:10.1038/ngeo1985, 2013.

- 1161 Li, J. and Zwally, H. J.: Modeling the density variation in the shallow firn layer, *Ann. Glaciol.*, 38(1),
1162 309–313, 2004.
- 1163 Ligtenberg, S. R. M., Medley, B., Van Den Broeke, M. R. and Munneke, P. K.: Antarctic firn
1164 compaction rates from repeat-track airborne radar data: II. Firn model evaluation, *Ann. Glaciol.*,
1165 56(70), 167–174, doi:10.3189/2015AoG70A204, 2015.
- 1166 Lipenkov, V. Y., Barkov, N. I., Duval, P. and Pimienta, P.: Crystalline texture of the 2083 m ice core at
1167 Vostok Station, Antarctica, *J. Glaciol.*, 35(121), 392–398, 1989.
- 1168 Loulergue, L., Parrenin, F., Blunier, T., Barnola, J.-M., Spahni, R., Schilt, A., Raisbeck, G. and
1169 Chappellaz, J.: New constraints on the gas age-ice age difference along the EPICA ice cores, 0-50 kyr,
1170 *Clim. Past*, 3, 527–540, 2007.
- 1171 Loulergue, L., Schilt, A., Spahni, R., Masson-Delmotte, V., Blunier, T., Lemieux, B., Barnola, J.-M.,
1172 Raynaud, D., Stocker, T. F. and Chappellaz, J.: Orbital and millennial-scale features of atmospheric
1173 CH₄ over the past 800,000 years, *Nature*, 453(7193), 383–386, doi:10.1038/nature06950, 2008.
- 1174 Lundin, J., Stevens, C., Arthern, R., Buizert, C., Orsi, A., Ligtenberg, S., Waddington, E., Firn Model
1175 Intercomparison Experiment (FirnMICE), *Journal of Glaciology*, 1–22. doi:10.1017/jog.2016.114,
1176 2017.
- 1177 Lüthi, D., Le Floch, M., Bereiter, B., Blunier, T., Barnola, J.-M., Siegenthaler, U., Raynaud, D., Jouzel,
1178 J., Fischer, H., Kawamura, K. and Stocker, T. F.: High-resolution carbon dioxide concentration record
1179 650,000–800,000 years before present, *Nature*, 453(7193), 379–382, doi:10.1038/nature06949,
1180 2008.
- 1181 Maeno, N. and Ebinuma, T.: Pressure sintering of ice and its implication to the densification of snow
1182 at polar glaciers and ice sheets, *J. Phys. Chem.*, 87(21), 4103–4110, 1983.
- 1183 Marcott, S. A., Bauska, T. K., Buizert, C., Steig, E. J., Rosen, J. L., Cuffey, K. M., Fudge, T. J.,
1184 Severinghaus, J. P., Ahn, J., Kalk, M. L., McConnell, J. R., Sowers, T., Taylor, K. C., White, J. W. C. and
1185 Brook, E. J.: Centennial-scale changes in the global carbon cycle during the last deglaciation, *Nature*,
1186 514(7524), 616–619, doi:10.1038/nature13799, 2014.
- 1187 Martinerie, P., Raynaud, D., Etheridge, D. M., Barnola, J.-M. and Mazaudier, D.: Physical and climatic
1188 parameters which influence the air content in polar ice, *Earth Planet. Sci. Lett.*, 112(1–4), 1–13,
1189 1992.
- 1190 Martinerie, P., Lipenkov, V. Y., Raynaud, D., Chappellaz, J., Barkov, N. I. and Lorius, C.: Air content
1191 paleo record in the Vostok ice core (Antarctica): A mixed record of climatic and glaciological
1192 parameters, *J. Geophys. Res. Atmospheres*, 99(D5), 10565–10576, 1994.
- 1193 Mellor, M.: Properties of snow, CRREL Monograph, Section III-A1., 1964.
- 1194 Miller, D. A., Adams, E. E. and Brown, R. L.: A microstructural approach to predict dry snow
1195 metamorphism in generalized thermal conditions, *Cold Reg. Sci. Technol.*, 37(3), 213–226,
1196 doi:10.1016/j.coldregions.2003.07.001, 2003.
- 1197 Morgan, V. I., High-temperature ice creep tests, *Cold Regions Science and Technology*, 19, 295-300,
1198 1991.

- 1199 Nie S., Bartelt, N. C. and Thürmer, K., Observation of Surface Self-Diffusion on Ice, *Physical Review*
 1200 *Letters*, PRL 102, 136101, DOI: [10.1103/PhysRevLett.102.136101](https://doi.org/10.1103/PhysRevLett.102.136101), 2009.
- 1201 Orsi, A. J., Cornuelle, B. D., & Severinghaus, J. P., Magnitude and temporal evolution of Dansgaard–
 1202 Oeschger event 8 abrupt temperature change inferred from nitrogen and argon isotopes in GISP2
 1203 ice using a new least-squares inversion, *Earth and Planetary Science Letters*, 395, 81-90, 2014.
- 1204 Overly, T. B., Hawley, R. L., Helm, V., Morris, E. M. and Chaudhary, R. N.: Greenland annual
 1205 accumulation along the EGIG line, 1959–2004, from ASIRAS airborne radar and detailed neutron-
 1206 probe density measurements, *Cryosphere Discuss.*, 9(6), 6791–6828, doi:10.5194/tcd-9-6791-2015,
 1207 2015.
- 1208 Parrenin, F., Dreyfus, G., Durand, G., Fujita, S., Gagliardini, O., Gillet, F., Jouzel, J., Kawamura, K.,
 1209 Lhomme, N., Masson-Delmotte, V., Ritz, C., Schwander, J., Shoji, H., Uemura, R., Watanabe, O., and
 1210 Yoshida, N.: 1-D-ice flow modelling at EPICA Dome C and Dome Fuji, East Antarctica, *Clim. Past*, 3(2),
 1211 243–259, 2007.
- 1212 Parrenin, F., Petit, J.-R., Masson-Delmotte, V., Wolff, E., Basile-Doelsch, I., Jouzel, J., Lipenkov, V.,
 1213 Rasmussen, S. O., Schwander, J., Severi, M., Udisti, R., Veres, D. and Vinther, B. M.: Volcanic
 1214 synchronisation between the EPICA Dome C and Vostok ice cores (Antarctica) 0-145 kyr BP, *Clim.*
 1215 *Past*, 8(3), 1031–1045, doi:10.5194/cp-8-1031-2012, 2012.
- 1216 Parrenin, F., Masson-Delmotte, V., Köhler, P., Raynaud, D., Paillard, D., Schwander, J., Barbante, C.,
 1217 Landais, A., Wegner, A., Jouzel, J.: Synchronous change of atmospheric CO₂ and Antarctic
 1218 temperature during the last deglacial warming, *Science*, vol. 339, 1060-1063, 2013.
- 1219 Pimienta, P.: Etude du comportement mécanique des glaces polycristallines aux faibles contraintes:
 1220 applications aux glaces des calottes polaires, PhD Thesis, Université Scientifique Technologique et
 1221 Médicale de Grenoble., 166 pp, 1987.
- 1222 Pimienta, P. and Duval, P.: Rate controlling processes in the creep of the polar glacier ice, *J. Phys.*
 1223 *Colloq.*, 48(C1), C1-243-C1-248, doi:10.1051/jphyscol:1987134, 1987.
- 1224 Proksch, M., Rutter, N., Fierz, C. and Schneebeli, M.: Intercomparison of snow density
 1225 measurements: bias, precision, and vertical resolution, *The Cryosphere*, 10(1), 371–384,
 1226 doi:10.5194/tc-10-371-2016, 2016.
- 1227 Ramseier, R. O.: Self-diffusion in ice monocrystals, CRREL Research Report no 232, 1967.
- 1228 Rasmussen, S. O., Andersen, K. K., Svensson, A. M., Steffensen, J. P., Vinther, B. M., Clausen, H. B.,
 1229 Siggaard-Andersen, M.-L., Johnsen, S. J., Larsen, L. B., Dahl-Jensen, D., Bigler, M., Röthlisberger, R.,
 1230 Fischer, H., Goto-Azuma, K., Hansson, M. E. and Ruth, U.: A new Greenland ice core chronology for
 1231 the last glacial termination, *J. Geophys. Res.*, 111(D6), doi:10.1029/2005JD006079, 2006.
- 1232 Rhodes, R. H., Brook, E. J., Chiang, J. C., Blunier, T., Maselli, O. J., McConnell, J. R., Romanini, D. and
 1233 Severinghaus, J. P.: Enhanced tropical methane production in response to iceberg discharge in the
 1234 North Atlantic, *Science*, 348(6238), 1016–1019, 2015.
- 1235 Salamatin, A. N., Lipenkov, V. Y., Barnola, J. M., Hori, A., Duval, P. and Hondoh, T.: Snow/firn
 1236 densification in polar ice sheets, *Phys. Ice Core Rec. - II*, 68(Supplement), 195–222, 2009.
- 1237 Schwander, J.: The transformation of snow to ice and the occlusion of gases, *Environ. Rec. Glaciers*
 1238 *Ice Sheets*, 53–67, 1989.

- 1239 Schwander, J., Barnola, J. M., Andrié, C., Leuenberger, M., Ludin, A., Raynaud, D., & Stauffer, B., The
1240 age of the air in the firn and the ice at Summit, Greenland. *Journal of Geophysical Research:*
1241 *Atmospheres*, 98(D2), 2831-2838, 1993.
- 1242 Schwander, J., Sowers, T., Barnola, J.-M., Blunier, T., Fuchs, A. and Malaizé, B.: Age scale of the air
1243 in the summit ice: Implication for glacial-interglacial temperature change, *J. Geophys. Res.*
1244 *Atmospheres*, 102(D16), 19483–19493, 1997.
- 1245 Severinghaus, J. P., Sowers, T., Brook, E. J., Alley, R. B. and Bender, M. L.: Timing of abrupt climate
1246 change at the end of the Younger Dryas interval from thermally fractionated gases in polar ice,
1247 *Nature*, 391(6663), 141–146, 1998.
- 1248 Sime, L. C., Wolff, E. W., Oliver, K. I. C. and Tindall, J. C., Evidence for warmer interglacials in East
1249 Antarctic ice cores, *Nature*, vol. 462, 2009.
- 1250 Sowers, T., Bender, M. and Raynaud, D.: Elemental and isotopic composition of occluded O₂ and N₂
1251 in polar ice, *J. Geophys. Res. Atmospheres*, 94(D4), 5137–5150, 1989.
- 1252 Sowers, T., Bender, M. and Korotkevich, Y.: $\delta^{15}\text{N}$ of N₂ in Air Trapped in Polar ice, *J. Geophys. Res.*,
1253 97(D14), 15–683, 1992.
- 1254 Veres, D., Bazin, L., Landais, A., Toyé Mahamadou Kele, H., Lemieux-Dudon, B., Parrenin, F.,
1255 Martinerie, P., Blayo, E., Blunier, T., Capron, E., Chappellaz, J., Rasmussen, S. O., Seeri, M., Svensson,
1256 A., Vinther, B., and Wolff, E. W.: The Antarctic ice core chronology (AICC2012): an optimized multi-
1257 parameter and multi-site dating approach for the last 120 thousand years, *Clim. Past*, 9(4), 1733–
1258 1748, 2013.
- 1259 WAIS Divide Project Members: Onset of deglacial warming in West Antarctica driven by local orbital
1260 forcing, *Nature*, 500(7463), 440–444, doi:10.1038/nature12376, 2013.
- 1261 WAIS Divide Project Members: Precise interglacial phasing of abrupt climate change during the last
1262 ice age, *Nature*, 520(7549), 661–665, 2015.
- 1263 Wilkinson, D. S. and Ashby, M. F.: Pressure sintering by power law creep, *Acta Metall.*, 23(11), 1277–
1264 1285, 1975.
- 1265 Witrant, E., Martinerie, P., Hogan, C., Laube, J. C., Kawamura, K., Capron, E., Montzka, S. A.,
1266 Dlugokencky, E. J., Etheridge, D., Blunier, T. and Sturges, W. T.: A new multi-gas constrained model
1267 of trace gas non-homogeneous transport in firn: evaluation and behaviour at eleven polar sites,
1268 *Atmospheric Chem. Phys.*, 12(23), 11465–11483, doi:10.5194/acp-12-11465-2012, 2012.
- 1269 Zwally, H. J. and Li, J.: Seasonal and interannual variations of firn densification and ice-sheet surface
1270 elevation at the Greenland summit, *J. Glaciol.*, 48(161), 199–207, 2002.